



Review

# Laser Additive Manufacturing of High-Strength Aluminum Alloys: Challenges and Strategies

Som Dixit and Shunyu Liu \*

Department of Automotive Engineering, Clemson University, Greenville, SC 29607, USA

\* Correspondence: shunyul@clemson.edu; Tel.: +1-864-365-0476

**Abstract:** Metal additive manufacturing (AM)-fabricated high-strength aluminum (HS-Al) alloys (2xxx, 6xxx, and 7xxx) tend to produce fatal metallurgical defects such as porosity and cracks. Since Al is the most important lightweight structural material in automotive and aviation industries, successful printing of HS-Al alloys is in high demand. Therefore, this review focuses on the formation mechanisms and research advancements to address these metallurgical defects. Firstly, the process optimization strategies, including AM parameter optimization, hybrid AM processes, and post-processing treatment, and their effectiveness and limitations have been reviewed thoroughly. However, process optimization can address defects such as porosity, surface roughness, and residual stresses but has limited effectiveness on cracking alleviation. Secondly, the research efforts on composition modification to address cracking in AM of HS-Al alloys are critically discussed. Different from process optimization, composition modification alters the solidification dynamics in AM of HS-Al alloys and hence is considered the most promising route for crack-free printing.



**Citation:** Dixit, S.; Liu, S. Laser Additive Manufacturing of High-Strength Aluminum Alloys: Challenges and Strategies. *J. Manuf. Mater. Process.* **2022**, *6*, 156. <https://doi.org/10.3390/jmmp6060156>

Academic Editors: Dong Lin, Kun Fu, Lei Chen and Mohamed A. Elbestawi

Received: 2 November 2022

Accepted: 5 December 2022

Published: 8 December 2022

**Publisher's Note:** MDPI stays neutral with regard to jurisdictional claims in published maps and institutional affiliations.



**Copyright:** © 2022 by the authors. Licensee MDPI, Basel, Switzerland. This article is an open access article distributed under the terms and conditions of the Creative Commons Attribution (CC BY) license (<https://creativecommons.org/licenses/by/4.0/>).

## 1. Introduction

High-strength aluminum (HS-Al) alloys, particularly 2xxx, 6xxx, and 7xxx, are revolutionizing automotive and aviation industries due to their high specific strength [1,2] and sustainable capabilities regarding pollution control and energy savings [3–5]; therefore, they are widely used as lightweight structural materials [6]. Traditional manufacturing of HS-Al alloys relies on thermomechanical processes (i.e., forging, stamping, forming, drawing) and casting [7], which have inherent limitations in material wastage and geometric constraints. Metal additive manufacturing (AM) is capable of addressing these limitations and provides new possibilities in geometry design [8] and multi-material development [9,10]. It uses a heating source (e.g., laser beam, electron beam, or arc beam) to melt powder or wire feedstocks layer-by-layer and fuses the melt pool into the three-dimensional (3D) part of a CAD model [11,12]. However, its unique thermal features (i.e., high cooling rates and large thermal gradients) make it compatible with only a few metals, such as titanium (Ti) alloys [13], stainless steel [14–16], superalloys [17,18], high entropy alloys [19] and tool steels [20].

AM of HS-Al alloys is challenging due to the prevalent cracks and porosity. HS-Al alloys are susceptible to hot cracking due to their extensive solidification range, high coefficient of thermal expansion, and low melt fluidity [21,22]. The required high energy input during AM of HS-Al alloys also tends to vaporize volatile alloying elements such as magnesium (Mg) and zinc (Zn) [23], which will further aggravate cracking and deteriorate the resultant mechanical properties [24]. Currently, among the various Al alloys, only the cast grade can be printed successfully without metallurgical defects [25] because of its higher silicon (Si) content that improves the melt pool's fluidity and helps backfill the regions prone to cracking [26]. Furthermore, cast Al alloys' solidification ranges are smaller

than those of high-strength Al alloys [27]. However, the relatively inferior mechanical properties of as-printed cast Al alloys over HS-Al alloys make them less favorable for structural applications [28,29].

Numerous research efforts have attempted to resolve the metallurgical defects—porosity and cracks—in AM of HS-Al alloys. The strategies are mainly focused on process optimization and composition modification. For process optimization, a high energy density that links the AM parameters (laser power, scan speed, layer thickness, and hatch spacing) is recommended for AM of HS-Al alloys [30,31]. The less energy input is prone to cause incomplete melting of Al alloys due to their high surface reflectivity and low absorptivity [30,32,33]. However, higher energy density is favorable for porosity reduction [31] but is less effective in cracking control [30]. Until now, Zhang et al. [34] successfully fabricated a crack-free 2xxx alloy using the energy density above the threshold value of 340 J/mm<sup>3</sup>. Scanning strategy is another crucial AM parameter to reduce porosity and cracks and alter microstructure [35,36]. The optimum selection of scanning strategy will reduce the formation of residual stresses and can alleviate the chances of crack formation but cannot eliminate it.

Additionally, incorporating hybrid processes such as laser remelting [37] and pre-heating [38] can improve printability in terms of higher density and fewer cracks. The laser remelting technique could effectively reduce porosity but could not eliminate cracks. Preheating the powder bed reduces crack formation significantly due to the reduction in thermal gradients and cooling rates [38]. Recently, a novel laser-arc hybrid additive manufacturing (LAHAM) process was developed to solve the cracking issues in AM of HS-Al alloys [39,40]. Results showed the complete elimination of cracks from single-track and multi-layer 2xxx and 7xxx alloys. The positive effects stem from the laser-arc hybrid process, which provides stability to the arc and improves the laser absorption rate of HS-Al alloys. Overall, altering the AM parameters, such as energy density and scanning strategy in process optimization, is less effective in addressing cracking issues [30,32,41]. While recent studies have demonstrated the effectiveness of hybrid AM processes in alleviating cracking issues, their effectiveness regarding large-scale parts is yet to be explored.

Compared with process optimization, composition modification is more effective in crack elimination and mechanical property enhancement. There are several ways to modify the composition, such as elemental powder mixture and the addition of alloying elements. Roberts et al. [42] showed that using optimal process conditions, the elemental combination of 99.5 wt.% Al and 0.5 wt.% Si can effectively reduce cracking compared with commercial AA6061 powders. The reduction in cracking was associated with congruent melting, which resulted in an almost single freezing point temperature instead of a freezing range. Therefore, the thermal stresses were eliminated, and hot tearing was avoided. Regarding cracking alleviation, the most common alloying elements added to HS-Al alloys are zirconium (Zr) [43,44], scandium (Sc) [45,46], Si [47,48], Ti [49,50], tantalum (Ta) [51], erbium (Er) [52], niobium (Nb) [53], and ceramic compounds [54,55]. These elements provide favorable metallurgical conditions during non-equilibrium solidification in metal AM processes, thus improving the printability of HS-Al alloys. For example, Wen et al. [56] showed that adding TiB<sub>2</sub> nanoparticles to AA2024 enhanced cracking resistance and mechanical properties by promoting the columnar-to-equiaxed transition (CET) mechanism. Similarly, the microalloying of Sc/Zr in the laser powder bed fusion (LPBF) fabricated HS-Al alloys leads to the formation of equiaxed grains due to the precipitation of Al<sub>3</sub>(Sc, Zr) phase and thus inhibits cracking [57].

The above discussion illustrates the substantial challenges in AM of HS-Al alloys and the potential strategies in recent research efforts. Therefore, a thorough review of the latest research breakthroughs regarding challenges and strategies is required. While a few review papers are about AM of Al alloys, to the authors' best knowledge, none focused on cracking mechanisms, cracking elimination strategies, and strategy effectiveness for AM of HS-Al alloys. For example, Aboulkhair et al. [28] discussed the LPBF processability of cast Al alloys regarding defect formation, microstructure, and mechanical properties. Still, it was

not related to HS-Al alloys. Zhang et al. [58] also studied the microstructural evolution and mechanical properties of AM-fabricated Al alloys, but the focus was on the Al-Si alloy series. Galy et al. [59] discussed the causes and consequences of the defects formed in the LPBF of Al alloys, including porosities, hot cracking, anisotropy, and surface roughness; however, their suppression mechanisms were not articulated. Aversa et al. [60] studied the inclusion of nanostructures in HS-Al alloys and their effects on microstructural evolution; however, new methodologies to improve the printability of HS-Al alloy, such as adding grain refiners and incorporating hybrid AM processes, were not mentioned. In a recent review by Kotadia et al. [61], the composition-dependent microstructural evolution and grain refinement mechanisms in the cast and HS-Al alloys were discussed, but the cracking mechanisms and crack-alleviation strategies were not included. Altiparmak et al. [62] discussed the recent progress in hybrid AM processes to fabricate HS-Al alloys. The study showed that hybrid AM could reduce porosity but cannot eliminate cracks.

This work will conduct a thorough literature review on cracking mechanisms and crack-alleviated strategies in AM of HS-Al alloys (i.e., 2xxx, 6xxx, 7xxx). The focus will be on the laser-based metal AM of HS-Al alloys, in which feedstock materials experience melting and solidification. In order to prevent duplication, the readers are encouraged to refer to the following literature for more details on different fusion-based metal AM processes [12,13,63]. The major findings of this paper are illustrated in seven sections. Section 2 covers the material selection criteria for metal AM processes and introduces representative Al compositions and their properties, as well as the promising Al alloys with good printability. Section 3 discusses the challenges in AM of HS-Al alloys, mainly focusing on the formation mechanisms associated with cracking and porosity. Sections 4 and 5 will thoroughly discuss the strategies—process optimization and composition modification—that can reduce defects, respectively. The conclusions drawn from this study are summarized in Section 6. Finally, an outlook is provided in Section 7.

## 2. Material Selection Criteria for Metal AM

### 2.1. Al Alloy Compositions and Properties

As there is a high emphasis on sustainable development, lightweight materials that can improve fuel efficiency and reduce gas emissions are gaining increasing attention in various industries, particularly for automotive, aerospace, and defense applications [13,28,64]. The most popular lightweight metals are Al, Ti, and Mg alloys. Table 1 summarizes their density, cost, applications, and limitations in automotive components. Compared with Ti alloys, Al alloys are lighter and much cheaper despite the lower strength-to-mass ratio. Mg is even lighter than Al, but it is easy to suffer from low creep resistance and galvanic corrosion. Overall, Al alloys are first-class lightweight materials with superior overall performances, and their demand in the transportation industry for structural applications has increased over time.

Table 2 summarizes the typical cast and wrought Al alloys and their representative compositions and properties [28]. Pure Al (1xxx) exhibits meager strength. Appropriate alloying elements must be added to enhance its strength. Depending on the primary alloying elements, Al alloys come in volatile grades but are generally classified into wrought and cast alloys [64]. Cast Al alloys are commonly produced by casting processes such as high-pressure die casting and investment casting [65]. These alloys mainly contain Si as a central alloying element, which helps in improving fluidity and castability. Wrought Al alloys generally have high formability and workability, good machinability, and high strength. Formability or workability refers to the ability to be fabricated into fashioning parts through mechanical deformation, which is less critical for metal AM processes. According to heat treatability, wrought Al alloys are grouped into non-heat-treatable (1xxx, 3xxx, 5xxx) and heat-treatable (2xxx, 6xxx, 7xxx) series [60,66]. Non-heat-treatable series is primarily hardened through mechanical treatment-induced forest dislocation strengthening. On the contrary, heat-treatable Al alloys are mainly strengthened via

precipitate hardening after aging heat treatment [67,68], which are widely used as structural materials for automotive and aviation industries due to their excellent strength and ductility.

**Table 1.** A general comparison among steel, Al, Mg, and Ti alloys for automotive applications.

	Density, g/cm <sup>3</sup>	Cost, \$/lb.	Applications	Limitations
Steel	7.75–8.05	0.35–0.42	The main body and chassis structural materials	High density, low strength-to-mass ratio
Al	2.7	1.6	Engine blocks, transmission casings, wheels, vehicle hoods, fenders (exterior components)	Lower strength than high-strength steels
Mg	1.74	2.7	Steering wheels, seat structures, instrument panels (interior components)	Low creep resistance, galvanic corrosion
Ti	4.51	30	Connecting rods, valves, camshafts, exhaust systems	High cost

**Table 2.** Properties and performances of typical compositions in each Al category [28,69].

Grade	Alloy #	Weldability	Castability	Heat-Treatability	Strength
Cast Al	AlSi10Mg	Excellent	Good	Yes	Medium
	AlSi7Mg	Excellent	Excellent	Yes	Medium
1xxx	1100	Excellent	Good	No	Low
	2011	Poor	Excellent	Yes	High
2xxx	2024	Poor	Good	Yes	High
	2618	Poor	Good	Yes	High
3xxx	3003	Excellent	Good	No	Medium
4xxx	4043	Excellent	Good	No	Medium
5xxx	5052	Good	Fair	No	Medium
6xxx	6061	Good	Good	Yes	Medium
	6063	Good	Fair	Yes	Medium
7xxx	7075	Poor	Fair	Yes	High
8xxx	8090	Fair	Fair	No	High

## 2.2. Material Properties Required for Fusion-Based Metal AM

The popular high-energy metal AM processes include powder-based LPBF [70,71], blown-powder directed energy deposition (DED) [72], electron beam melting [73,74], and wire-based arc additive manufacturing [75]. During AM processes, the heating source interacts with metallic feedstocks and creates a melt pool in each single-track scan is produced. The highly localized heat input and short interaction time will produce high cooling rates and large temperature gradients [13]. This highly non-equilibrium thermal history will provide different and unfavorable thermodynamic and kinetic behaviors, which necessitate the material candidates with unique properties to ensure a good printability with reduced defects. In general, the material selection criteria for metal AM should consider weldability, castability, heat treatability, mechanical properties (for structural applications), and economic effectiveness. It should be noted that all these considerations could only increase the probability but cannot guarantee a successful print.

Weldability is the ultimate vital property to ensure good printability since the nature of metal AM is defined as a form of a multi-pass micro-welding process with preset scan strategies [28]. However, welding is generally applied to a seam, and filling material may be used. In other words, the weldability may be improved depending on the base and filler materials. Castability is the second vital property to project good printability since the feedstock materials experience melting and resolidification during metal AM and casting processes. The primary difference between AM and casting lies in the more extreme thermal features (i.e., higher cooling rate and larger temperature gradient) of metal AM than casting. Generally, excellent weldability and castability could reduce defects such as shrinkage pores and thermal cracks after a rapid heating and cooling cycle. Heat treatability is another

critical property for selecting a suitable AM material because the as-printed material tends to experience property degradation due to the formed anisotropic microstructure [13,76–79] and defects [58,59,62]. Therefore, heat treatment becomes a necessary strategy to recover the mechanical properties of AM parts.

In addition to the abovementioned three properties, mechanical properties also play an important role in material selection since they directly determine the performance and applications of the final products. After AM processing and post-heat treatment, the qualified materials are expected to have improved mechanical properties or little property deterioration. Based on the discussion of the desired material properties for fusion-based metal AM, several Al alloys have demonstrated high compatibility with different laser AM methods. These Al alloys offer defect-free printing in their original compositions. Table 3 summarizes these Al alloys, corresponding AM methods, and their printing conditions. Detailed discussions will be covered in the following sections.

**Table 3.** Printable Al alloys and their corresponding AM methods.

Al Alloys	AM Methods	Conditions	References
AlSi10Mg	LPBF, DED	As printed	[80,81]
AlSi7Mg	LPBF	As printed	[82]
Al7Si0.6Mg	LPBF	As printed	[83]
AlSi12Mg	LPBF	As printed	[84]
AA6061	Hybrid AM	Powder-bed preheating	[38]
AA2219	Hybrid AM	Single track	[39]
AA7075	Hybrid AM	Singlettrack	[40]

### 2.2.1. Suitable Al Alloys for Metal AM Processes—Cast Al Alloys

Based on the material selection criteria for metal AM, the soundest Al alloys should be the cast grade Al-Si-MgCuZn [85]. Until now, cast Al-Si alloys, e.g., AlSi10Mg [80,86–89], AlSi7Mg [82,83], and AlSi12Mg [84] have been widely studied for different AM processes, and solid AM parameters have been identified. The better AM processability of cast Al alloys than HS-Al alloys is due to the formation of eutectic composition, higher Si content, and lower solidification range. Moreover, low melting point phases will provide extra liquid feeding and resist crack formation by filling the gaps between interdendritic films [61]. Figure 1 presents the microstructure of AlSi10Mg printed by the 3D SYSTEMS DMP printer. The part is free from cracks, and the density is up to 99.3%. However, cast Al-Si alloys generally have lower mechanical properties than HS-Al alloys. Table 4 summarizes the mechanical properties of die-casting AlSi10Mg as compared with the LPBF counterparts and the wrought AA6061 alloy. Compared with AA6061 alloy after T6 aging treatment, the die-casting AlSi10Mg has a much lower yield strength and ductility. The as-printed AlSi10Mg alloys are broadly reported to have higher strength than their cast counterparts [87,90–94] (Table 4). The underlying reason is associated with the as-solidified microstructure that exhibits a cellular structure with Si precipitating at the grain boundary, thereby increasing the strength by impeding the dislocation motion [88]. Moreover, the dislocation networks formed in the solidification cells contribute to dislocation hardening [95]. Applying solution heat treatment will coarsen grains and relieve residual stresses while trading off the high strength; therefore, the heat treatment does not improve the performance of AlSi10Mg parts.

**Table 4.** Mechanical properties of the LPBF-built and cast AlSi10Mg after solution and T6 aging heat treatment compared with wrought counterparts and AA-6061 alloys.

Manufacturing Condition	YS, MPa	UTS, MPa	$\varepsilon_{break}$ , %	Reference
As-built LPBF AlSi10Mg	$322.17 \pm 8.1$	$434.25 \pm 10.7$	$5.3 \pm 0.22$	[87]
As-built LPBF AlSi10Mg after 450 °C solution for 2 h	$196.58 \pm 3.6$	$282.36 \pm 6.1$	$13.4 \pm 0.51$	[87]

**Table 4.** Cont.

Manufacturing Condition	YS, MPa	UTS, MPa	$\varepsilon_{\text{break}}, \%$	Reference
As-built LPBF AlSi10Mg after 500 °C solution for 2 h	$126.00 \pm 2.1$	$213.75 \pm 4.6$	$23.5 \pm 0.81$	[87]
As-built LPBF AlSi10Mg after 550 °C solution for 2 h	$90.52 \pm 1.6$	$168.11 \pm 2.4$	$23.7 \pm 0.84$	[87]
High-pressure die casting	175	300–350	3–5	[96]
High-pressure die casting after T6 aging heat treatment	-	330–365	3–5	[97]
Wrought AA6061-O	55	124	30	[98]
Wrought AA6061 after T6 treatment	276	310	12	[98]

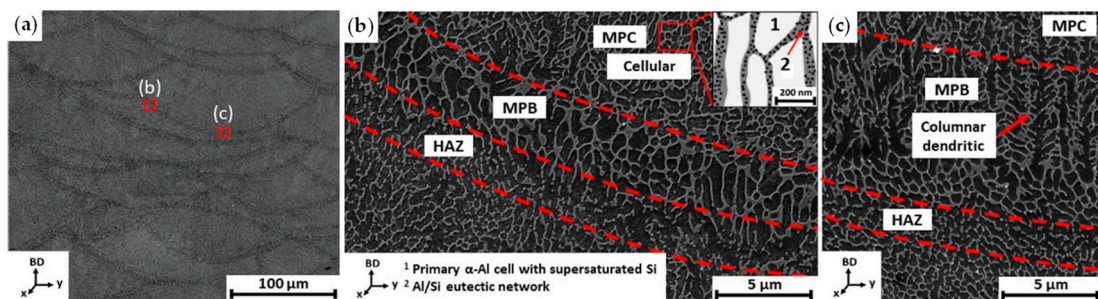


**Figure 1.** SEM images of cast Al alloy—AlSi10Mg printed by the 3D SYSTEMS DMP printer: (a) As-printed overall microstructure shows a high density. Microstructural details reveal (b) cellular grains at the melt pool center (MPC) and (c) columnar dendritic grains at the melt pool boundary (MPB) and heat-affected zone (HAZ). Reproduced with permission from Springer Nature [95].

### 2.2.2. Suitable Al Alloys for Metal AM Processes—6xxx Series Al Alloys

According to the material selection criteria for metal AM, 6xxx series Al alloys are also promising candidates due to their good weldability, reasonable castability, heat treatability, and superior overall mechanical properties. Indeed, AM of the 6xxx series (e.g., AA6061) is gaining increasing attention from various industries and is intensively studied by researchers from the AM community [42]. Currently, laser welding of AA6061 is successful regardless of the filling materials. As shown in Figure 2, for the joint welding of 4 mm thick 6061 plates, the seam is free from cracks and pores. However, when subjected to the AM process, AA6061 experiences thermal cracking issues [38,42] (Figure 3). Cracking is associated with the thermal features of AM process, such as high cooling rates and large thermal gradients, which promote the formation of long columnar grains along the scan and build directions, making them more prone to solidification cracks [28]. Therefore, it is readily seen that weldability is necessary but insufficient for metal AM of HS-Al alloys. The underlying reasons associated with the limitations in AM of 6061 and other HS-Al alloys, i.e., 2xxx and 7xxx, will be discussed in the “Challenges” section. The effective strategies to address these challenges will be presented in the “Strategies” sections.

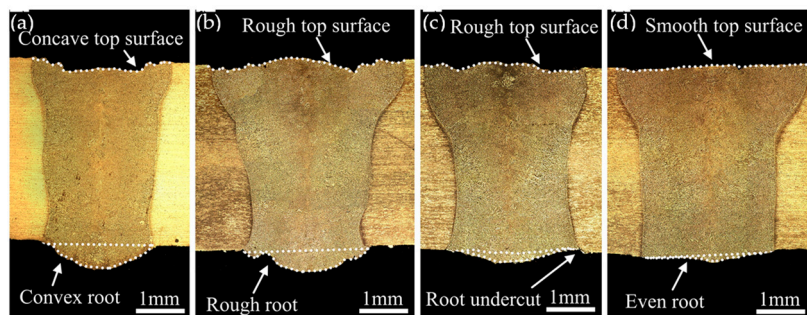


**Figure 2.** Weld seam and corresponding cross-section morphologies of the joint welding of 4 mm thick AA6061 plates: (a) without oscillation; (b) transverse oscillation; (c) longitudinal oscillation; (d) circular oscillation. Reproduced with permission from Elsevier [99].

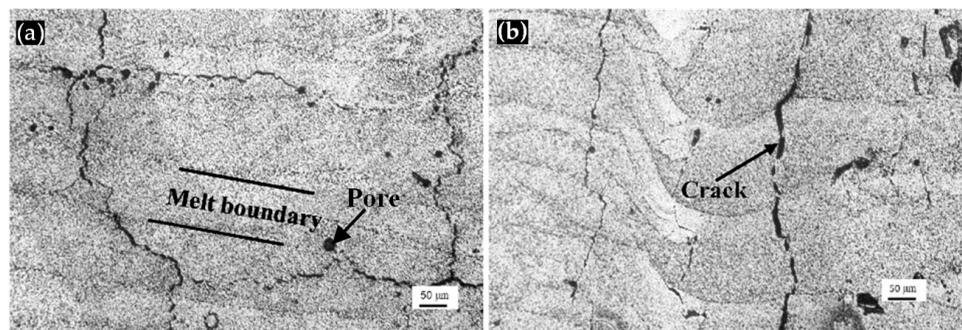


**Figure 3.** Microstructure of the LPBF-fabricated AA6061: (a) XY plane (perpendicular to build direction); (b) ZX plane (build direction). Reproduced with permission from Elsevier [38].

### 3. Challenges in AM of HS-Al Alloys

Challenges regarding the poor printability of HS-Al alloys are primarily related to the formed metallurgical defects, including cracking, porosity, oxidation, element vaporization, balling, and satellite generation, among which cracking and porosity are most disastrous. The underlying reasons associated with the cracking in AM of high-strength Al alloys are majorly attributed to the elongated grain structure, large freezing range, high coefficient of thermal expansion, and oxide film [100–102]. Differently, the presence of moisture is the primary reason behind porosity in Al alloys due to Al affinity towards oxygen [103]. This review paper will focus on the dominant defects—cracking and porosity—in AM of HS-Al alloys. Concerning the common defects in metal AM processes, such as residual stresses, non-equilibrium microstructure, and anisotropy, please refer to Refs. [58,59,62].

#### 3.1. Cracking

Hot cracking or solidification cracking is common in AM-processed HS-Al alloys. For example, Zhang et al. [104] reported long cracks along grain boundaries of large columnar grains towards the build direction in the LPBF-fabricated Al-Cu-Mg alloy. A similar crack morphology was also observed in the LPBF of 7075 [30]. The primary factors leading to hot cracks in AM of HS-Al alloys are summarized in Figure 4.

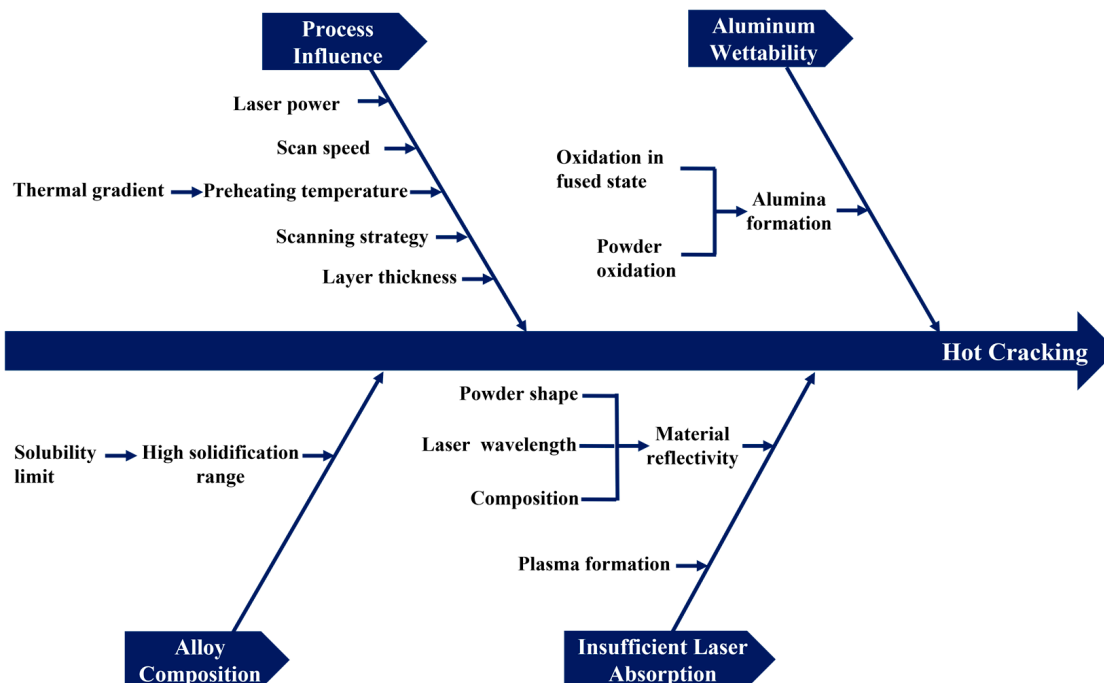


**Figure 4.** Different causes for the formation of hot cracking in metal AM of HS-Al alloys.

Cracking in AM of Al alloys is divided into two categories, i.e., liquation and solidification cracking [105]. Liquation cracking selectively happens to the low melting point substances in the matrix or segregates at grain boundaries. During heating cycles, these regions first melt locally and destroy the main body's integration, becoming the crack initiation points. Conversely, solidification cracks, also known as thermal cracks or hot tears, occur during the solidification stage rather than in the melting cycle. They are formed when insufficient backup liquid is left to fill the gaps between the solidified metal during solidification shrinkage [62].

Despite the different features of liquation and solidification cracking, they share the same feature of separating the continuous materials by generating a weak point. Liquation cracking is thus considered a vital initiation site for solidification cracking [106]. For cracks initiating along the grain boundary and propagating at the interdendritic liquid film, the grains separate along the lateral direction due to the tensile strain. Li et al. [107] discussed the role of strain theory in the rupture of the liquid film in the interdendritic region when the strain reaches a threshold value. If the lateral growth of grains and liquid feeding along grain boundaries fail to compensate for the local strain's negative influence, the materials are characterized by high cracking susceptibility. Soysal et al. [108] used the maximum steepness [ $dT/d(f_s)^{1/2}$ ] of the  $T-(f_s)^{1/2}$  curve to describe the cracking susceptibility of several representative high-strength Al alloys, where  $T$  is solidification temperature, and  $f_s$  is solidified fraction. Generally, a larger steepness indicates a higher cracking susceptibility. As seen in Figure 5, the steepness peaks are formed at the terminal stage of solidification when  $f_s$  is close to 1, which confirms the occurrence of solidification cracking due to the lack of backup liquid. Among all studied HS-Al alloys, 6061 has the highest susceptibility for solidification cracking, followed by 7075 and 2xxx alloys.

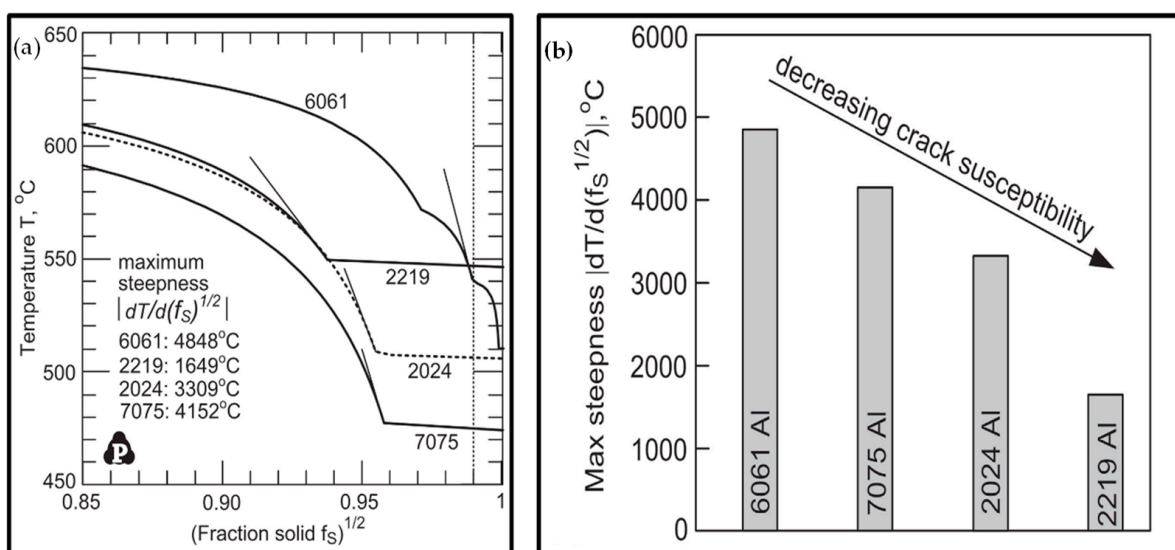


**Figure 5.** Crack susceptibility of HS-Al alloys: (a)  $T-(f_s)^{1/2}$  curve showing maximum steepness; (b) steepness variations of different Al alloys. Reproduced with permission from Elsevier [108].

One general factor for the prevalent cracks in AM metals is related to grain misorientation [109]. AM parts have a unique grain texture that features columnar grains spanning over many layers along the build direction [13,76–79]. The formation of columnar grains stems from a lack of sufficient undercooling for nucleation at the solidification front in a continuously formed melt pool. Since the heat in the molten pool is primarily dissipated downwards through the substrate, grains grow epitaxially along the maximum temperature gradient during the deposition of subsequent layers [110,111] and hence form low-angle grain boundaries. Since solidification cracks always propagate along grain boundaries, they are therefore oriented towards the build direction. As illustrated in Figure 6, long columnar grains have a smaller dihedral angle ( $\emptyset$ ) than short columnar grains and equiaxed grains.

The resultant deeper channel between low-angle grain boundaries adds difficulty for liquid feeding [44]; therefore, AM-generated columnar grains are inherently more susceptible to cracking than equiaxed grains.

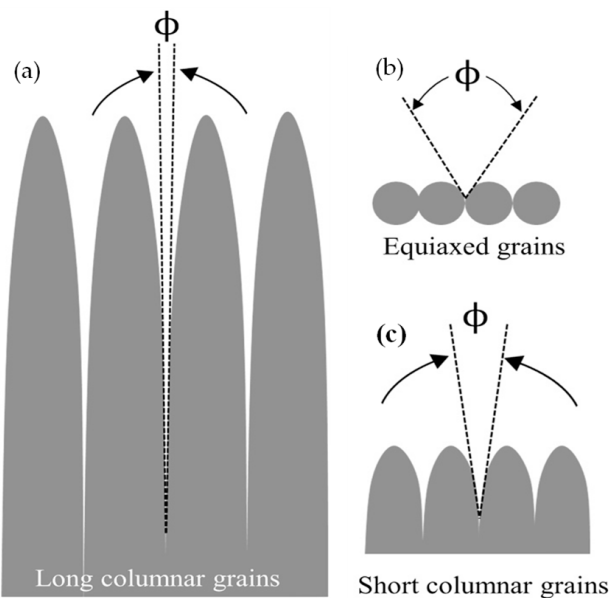


**Figure 6.** Schematic illustration of dihedral angles between (a) long columnar grains; (b) short columnar grains; (c) equiaxed grains. Reproduced with permission from Elsevier [44].

Additionally, materials with a large solidification (freezing) range, known as the difference between liquidus and solidus temperatures, tend to favor the formation of liquation cracking [101,112]. The negative effect of the large solidification range is associated with the formed complex dendritic structures in the mushy zone, which will retard the transport of liquid metal to the shrinkage area. Figure 7 shows the solidification ranges of the representative 2xxx, 5xxx, 6xxx, and 7xxx HS-Al alloys. Since 2024 and 7075 have larger solidification ranges than 6061, they should be more prone to solidification cracking. However, this contradicts the crack susceptibility in Figure 5. One main reason is that the crack susceptibility graph (Figure 5) only demonstrates the terminal stage of solidification, which is less representative of the entire solidification range. Anyway, additional reasons other than the solidification range will also account for the crack susceptibility, which will be discussed as follows.

Oxidation is another primary reason for the prevalent cracks in AM-printed Al alloys. Al alloys are one of the most reactive metals with a high affinity for oxygen and moisture. During metal AM processes, the atmosphere must be well controlled to reduce the oxygen and moisture level; otherwise, hard and brittle Al oxides will be formed. Louvis et al. [85] studied the LPBF of 6061, and the as-printed part was plagued with a low density of 89.5% and extensive cracks. The presence of oxide film between layers was considered to be the reason for delamination and subsequent crack propagation between layers. It was claimed that this high melting-point oxide film broke down in the melt pool during the printing of subsequent layers but could not be melted completely due to its high melting point. During the subsequent solidification of the melt pool, this oxide will be embedded in the fused deposition or between layers, breaking the material's continuity and weakening the bonding force. The oxygen pickup by the precursor powders during recycling is also a source of the high oxygen concentration [103]. Therefore, Al recycling is less favored compared with other non-reactive powders.

Another critical factor accounting for the prevalent cracks in AM-printed Al alloys is the unique thermal property of Al alloys, which will lead to unfavorable thermal histories during AM processes. Due to Al's high thermal conductivity and reflectivity, an exceptional high-energy input is required to melt Al powders; otherwise, a lack of fusion porosity will

form, which acts as a site for crack nucleation and propagation. Additionally, the absorbed energy will be quickly dissipated due to the high conductivity, imparting a significant thermal gradient and corresponding thermal stresses, creating a favorable environment for solidification cracking [113].

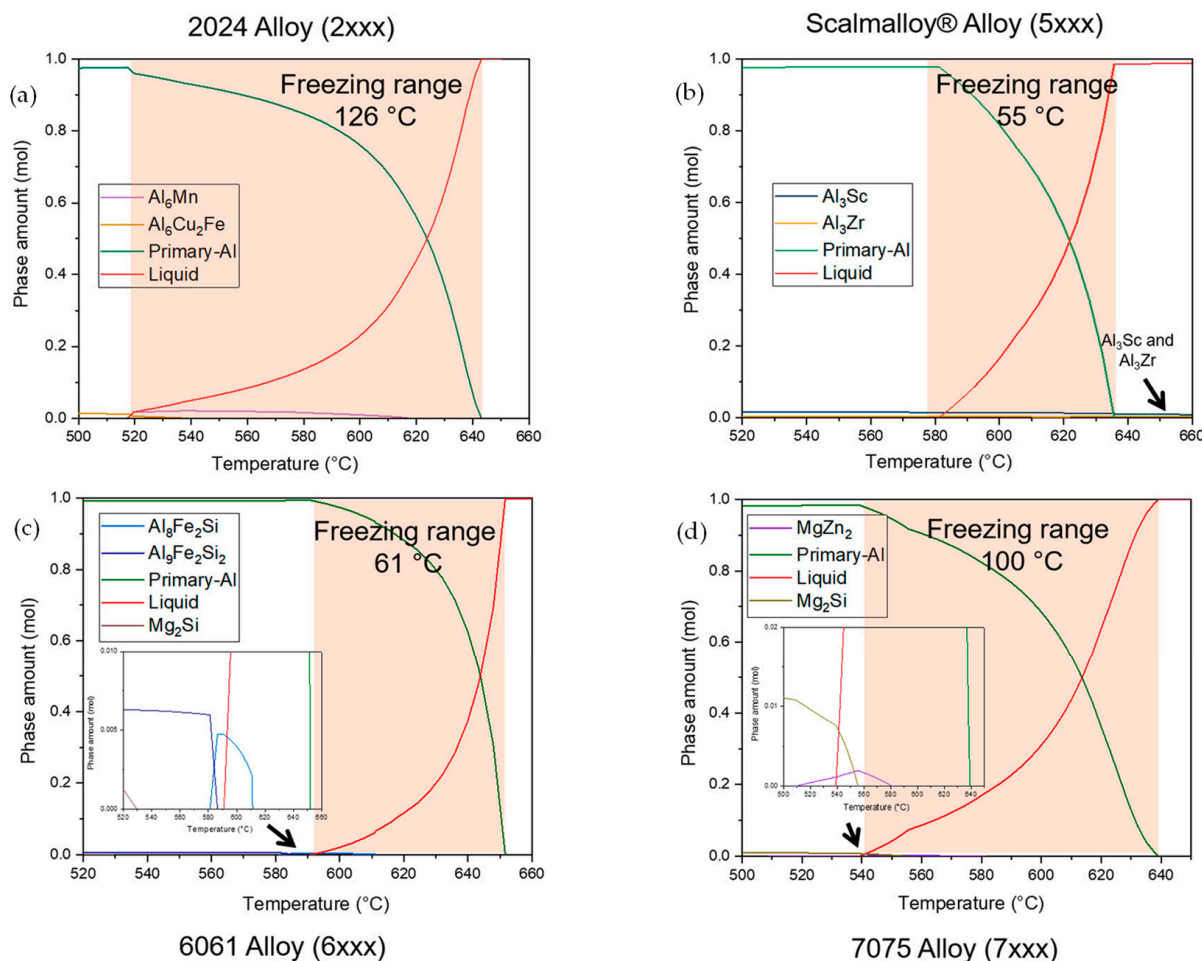


**Figure 7.** Thermo-Calc generated graphs for the solidification ranges of (a) 2024; (b) Scalmalloy<sup>®</sup>; (c) 6061; (d) 7075 alloys. Reproduced with permission from Elsevier [61].

### 3.2. Porosity

Compared with common AM metals, AM of Al alloys is particularly sensitive to pore formation. Porosity is defined as the volume percent of pores present in the sample. Generally, the porosity formation in all AM metals is divided into two categories: fusion pores and gas pores [58]. Fusion pores are formed by insufficient energy supply, which causes incomplete melting of powder particles. These pores are generally irregular and large (several hundred microns). The gas pore is formed due to the entrapment of gas molecules within the melt pool beyond solubilities. These gases may be produced due to chemical reactions during AM processes and from the source of an inert atmosphere. Moreover, high laser power is required for AM of Al alloys due to Al's high thermal conductivity and reflectivity. Therefore, fusion pores are prevalent when inappropriate parameters result in an insufficient energy density (Figure 8). However, excessively high energy will cause the evaporation of alloying elements and may lead to the formation of gas pores.

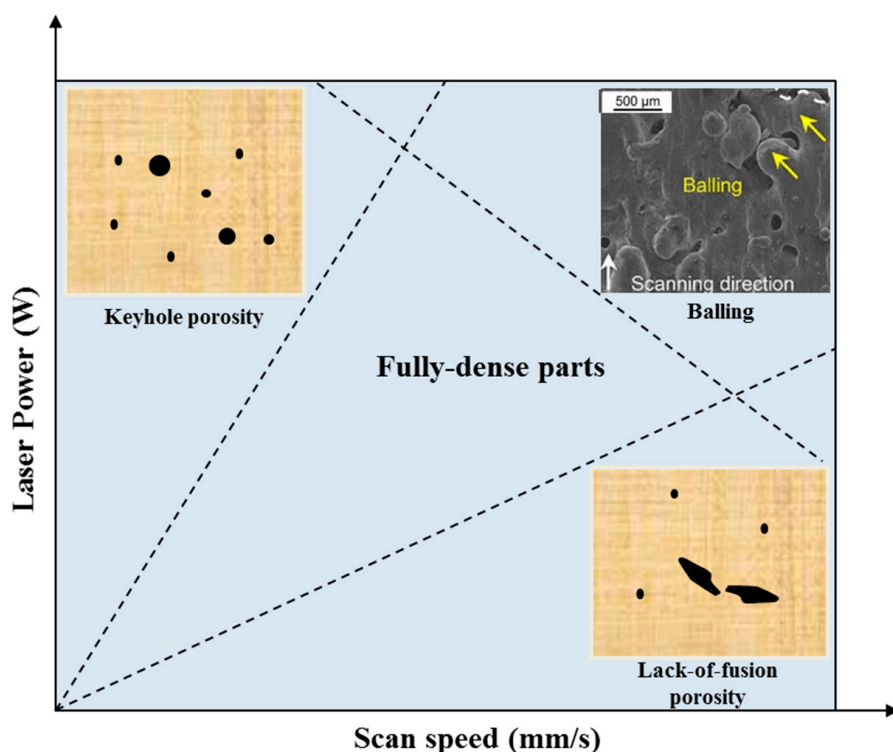


**Figure 8.** Influences of laser power and scanning velocity on porosity. Reproduced with permission from Elsevier [70,114].

Another critical source of porosity in AM of Al alloys is the hydrogen (H) pickup [115]. During the heating cycle, the high temperature induced by the laser energy will decompose moisture into H, and the melt pool will be enriched with H. Since the solubility of H in liquid Al is much higher than that of solid Al, H atoms will be rejected from the fused metal and form H gases in the deposition. Additionally, the high energy input during AM of Al alloys is easy to form a key-hole mode [28], where the Marangoni force tends to drive the H gas to the bottom of the melt pool [115]. Along with a fast solidification rate resulting from a high scan speed, the H gas will have less time to escape from the melt pool, significantly increasing the chance of pore formation.

To counter the effect of H pickup in the melt pool, Weingarten et al. [116] suggested proper powder cleaning and drying. Yang et al. [115] also proved that drying powder particles before processing will reduce porosity in AM of Al parts by a significant amount. Dai et al. [117] also discussed the effect of different shielding gases on melt pool dynamics. Results showed that argon (Ar) and nitrogen (N<sub>2</sub>) lead to a more uniform recoil pressure and a more stable melt pool compared with helium (He) gas.

#### 4. Strategies to Improve Printability of HS-Al Alloys—Process Optimization

This section will comprehensively review the processing capabilities in alleviating defects, including AM parameter optimization, hybrid AM processes, and post-processing treatment. Their effectiveness and limitations in eliminating or reducing the defects, such as porosity, cracking, surface roughness, and residual stresses, will be thoroughly discussed. Regarding AM parameter optimization, all the AM parameters will be studied. In addition to the scanning strategy, all other AM parameters will be synergistically considered through the parameter of energy density. In general, optimizing AM parameters have little to do with cracking alleviation. Therefore, the emerging hybrid AM processes, and the popular post-processing treatment will also be introduced.

#### 4.1. AM Parameter Optimization

##### 4.1.1. Energy Density

AM process involves multiple parameters. In addition to the scanning strategy, the synergistic effect of all other AM parameters, including laser power ( $P$ ), scan speed ( $V$ ), hatch spacing ( $H$ ), layer thickness ( $T$ ), and laser absorptivity ( $\alpha$ ), is commonly studied using the parameter of volumetric energy density ( $E_{Vol} = P\alpha / VHT$ ). Since Al generally has a low absorptivity coefficient but a very high reflectivity regarding the standard laser wavelengths for metal AM, printing Al requires a high laser power and a low scan speed. It is worth noting that an optimized printing condition and a relatively high energy density will produce a high-density part free from cracks for most printable metals [118,119]. However, for most HS-Al alloys, optimization of AM parameters can only reduce porosity rather than cracking. Pekok et al. [31] investigated the effect of energy density on the processability of the LPBF-fabricated AA-2024 while keeping layer thickness constant. Under optimal conditions, a successful printing produced a high density of up to 99.8%, but minor cracks were still observed.

Similar studies were carried out on 6061 [33,120] and 7075 [32,41] in terms of energy density optimization that correlates with part density, dimensional accuracy, surface roughness, and crack formation. The optimum energy density for minimizing cracks in AM 6061 is around 55–70 J/mm<sup>3</sup> [121], while 7075 is about 83.3 J/mm<sup>3</sup> [48]. However, none of these studies could eliminate cracks in AM of commercial HS-Al alloys [30,32,41]. In addition to commercial compositions, exciting research by Zhang et al. [34] on the LPBF of Al-Cu-Mg (belongs to the 2xxx series) alloy has solved the cracking issue. This work focused on the densification of printed samples by adjusting the volumetric energy density. Above the threshold value of 340 J/mm<sup>3</sup>, the printed samples were 99.8% dense without any porosity or solidification cracks. It is essential to highlight that the improved printability may be due to the modified composition, which will be discussed in detail in Section 5.

##### 4.1.2. Scanning Strategy

The scanning strategy is defined as the path that laser traces over the powder bed or during the deposition process. The selection of optimum scanning strategy influences the porosity formation, microstructure evolution, and residual stresses in AM of Al alloys. Residual stress is one of the dominant factors for crack formation in AM-fabricated parts. Residual stresses are produced due to AM's large thermal gradients and high solidification rates [28].

Different scanning strategies were explored to reduce residual stresses, which ultimately reduced the thermal gradient in AM process. For example, Lu et al. [122] showed that incorporating the island strategy effectively reduced the residual stresses by dividing each layer into smaller tracks and shortening the length of a single scan track. Moreover, varying the island sizes based on the scan vector affects the crack and pore formation from the LPBF-fabricated Inconel-718 alloy. Chen et al. [123] illustrated that increasing the overlap between island borders in a 25–50% range would also reduce the residual stress in the x-direction for the LPBF-fabricated Ti6Al4V. In the case of Al alloys, Koutny et al. [36] demonstrated the effectiveness of using a meander and island scanning strategy on the cracking behavior of AA2618. Results showed that scanning strategies could not effectively eliminate cracks. Although the scanning strategy reduces the residual stresses, other factors, such as the large solidification range and low melt fluidity in AM of HS-Al alloys, will remain unaffected. Therefore, to reduce cracking in HS-Al alloys, the solidification thermodynamics needs to be changed [101], which will be discussed in detail in Section 5.

#### 4.2. Hybrid AM Processes

Hybrid AM is the use of AM with one or more secondary processes or energy sources that are fully coupled and synergistically affect part quality, functionality, and/or process performance [124], which is not limited to additive plus subtractive processes. Since optimizing AM processes solely fails to eliminate cracking in commercial HS-Al alloys,

recent research efforts seek assistance from hybrid processes by incorporating a beneficial second heat source or process with AM processes. One effective method to prevent cracking is preheating. Uddin et al. [38] successfully solved the cracking problem by heating the powder bed to a high temperature of 500 °C, as shown in Figure 9. Table 5 summarizes the mechanical properties of AM-built preheated AA6061 after T6 aging compared with wrought counterparts. The positive effect of preheating lies in the reduced cooling rate and relieving residual stresses. Preheating also reduces moisture in precursor Al powders, reducing porosity and cracks associated with H absorption.

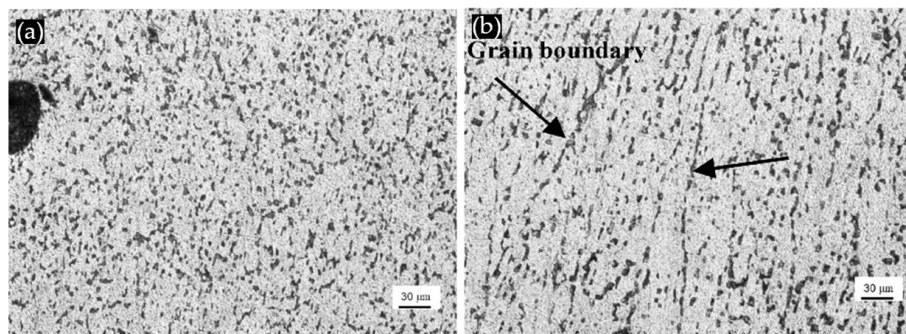


**Figure 9.** Microstructure of AA6061 fabricated with preheated laser powder-bed at 500 °C: (a) XY plane; (b) ZX plane (build direction). Reproduced with permission from Elsevier [38].

**Table 5.** Mechanical properties of the LPBF-built and cast AA6061 after annealing and T6 aging heat treatment. YS is yield strength, UTS is ultimate tensile strength, and  $\varepsilon_{\text{break}}$  is the elongation at fracture.

Manufacturing Condition	YS, MPa	UTS, MPa	$\varepsilon_{\text{break}}$ , %	Reference
Heated powder bed-LPBF-built AA6061	70.5	137	13	
Heated powder bed-LPBF-built AA6061-T6	286	313	4.45	
Wrought AA6061-O	55	124	30	
Wrought AA6061 after T6 treatment	276	310	12	[38]

Porosity can also be reduced by using an oscillating laser beam instead of a linear beam. Figure 10 demonstrates the effect of different oscillating laser beam files on porosity [125]. It is readily seen that the infinity oscillating path showed the best response in terms of reduced porosity, and it is attributed to the formed steady key-hole mode during laser welding. Although this study does not focus on welding, a similar strategy could also be applied to AM processes.

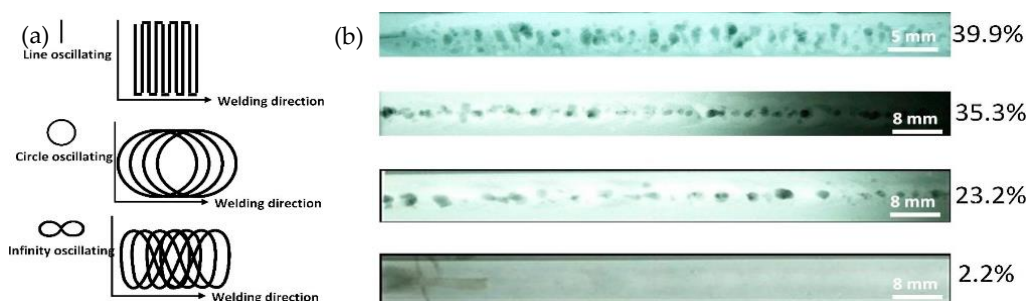


**Figure 10.** (a) Oscillating laser beam profile; (b) Porosity variation with different beam profiles. Reproduced with permission from Elsevier [125].

Concerning the second heat source, remelting finds its wide application in reducing porosity. Through this process, the laser beam passes over each layer after the layer has already solidified and remelts the layer. The liquid metal will fill the pores during remelting

and improve surface quality. Optical micrographs of the LPBF parts with and without laser remelting are shown in Figure 11 [37]. It was found that the surface roughness went down from 12  $\mu\text{m}$  to 1.5  $\mu\text{m}$  by introducing remelting passes. The relative porosity was reduced from 0.77% to 0.036%. A similar methodology can also be applied to Al alloys. Yu et al. [126] investigated the effect of laser remelting on the surface roughness and porosity of AlSi10Mg fabricated by the LPBF process. Results showed that remelting decreases the surface roughness from 20.67  $\mu\text{m}$  to 10.87  $\mu\text{m}$ . Moreover, remelting allows the spherical pores to escape from the melt pool. A similar improvement in surface roughness due to remelting in AM of Al alloys was observed in other studies [127,128]. However, none of the studies related to remelting can address cracking in AM of HS-Al alloys.

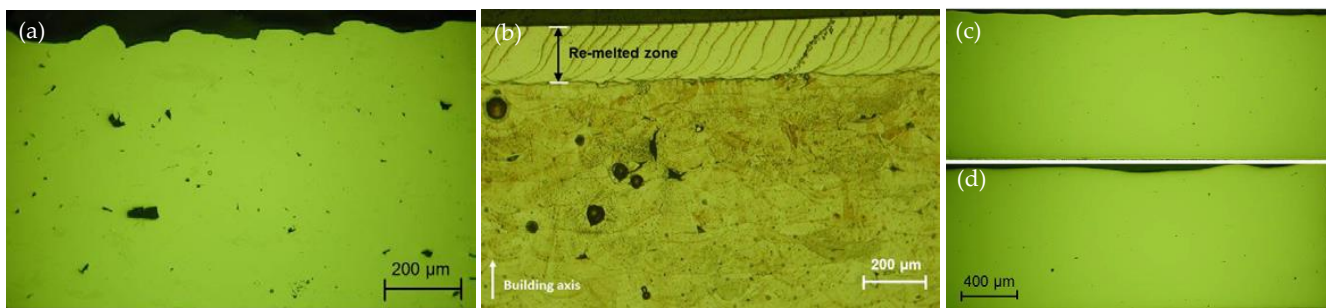


**Figure 11.** Microstructure of the LPBF-printed 316L stainless steel: (a) The as-printed part shows a high surface roughness; (b) the as-printed part with remelting of the top layer; (c) One remelting scan reduces porosity to 0.036%; (d) Three remelting scans produce 0.043% porosity. Reproduced with permission from Elsevier [37].

Apart from incorporating a secondary heat source into the existing AM methods, there are several attempts in which a secondary process is added by doing process hybridization. Wu et al. [39] fabricated the Al-Cu (AA2219) alloy using a novel hybrid-AM process, where pulsed laser and TIG process were combined and called laser-arc hybrid-AM (LAHAM). Results showed no cracks on the cross-section view and improved mechanical properties of the fabricated part. The improved printability and mechanical properties are related to the refined grain structure, uniform Cu distribution, and small eutectics in the fusion zone. Similarly, Liu et al. [40] have incorporated the LAHAM to fabricate the crack-free 7xxx Al alloys. 7xxx series offer limited manufacturing potential for AM due to the cracking issue, which is attributed to the significant Zn vaporization during the AM process, resulting in the loss of Zn element up to 30.8%. In the LAHAM process, the Zn loss is reduced to 2.3%. Zn is the primary strengthening element for the 7xxx series. Apart from the reduced element vaporization, the LAHAM process provides grain refinement and reduced <100> texture along the build direction. Moreover, the even distribution of AlZnMgCu-eutectics and the formation of nano precipitates also contribute to the higher mechanical properties.

It should be noted that despite the promising results, hybrid AM processes are still in their infancy. It is still an open question whether they have the universal capability to address cracking and porosity for different HS-Al alloys. Additionally, the current studies of hybrid AM processes of HS-Al alloys are primarily focused on single-track or several-layer samples. Although the current fabrication route does not show any metallurgical defects, it is required for scale-up investigation and validation. However, the current methodology can effectively eliminate surface defects in HS-Al alloys for surface modification and coating applications.

#### 4.3. Post-Processing Treatment

The post-processing treatment is essential in eliminating or reducing defects such as porosity, surface roughness, and residual stresses of the as-printed HS-Al alloys. The two main post-processing techniques are surface treatment and heat treatment. Surface treatment that implements peening, remelting, and milling is one of the critical post-processing

techniques to alleviate defects and improve microstructure. In shot peening and laser shock peening, compressive force is applied at the surface by accelerated spherical media (e.g., metallic balls) or an intense pulsed laser beam, resulting in plastic deformation at the deposition surface [124]. Implementing the peening techniques reduces porosity and improves the AM parts' fatigue performance by introducing compressive residual stresses and inhibiting crack initiation and propagation. For example, Damon et al. [129] investigated the influence of shot peening on the porosity reduction in the LPBF-fabricated AlSi10Mg. Results showed a significant decrease in porosity at the top surface up to 500  $\mu\text{m}$ . Moreover, considerable shrinkage of pores was observed along with the change in pore orientation. Apart from peening, laser remelting in a hybrid AM process can be used to improve the printed parts' surface finish, which was discussed in detail in Section 4.2. Another aspect of surface treatment can be achieved by incorporating machining and abrasive finishing methods, which can significantly improve the surface finish of the printed parts. For example, Teng et al. [130] studied a combination of the grinding process and magnetic abrasive finishing to reduce surface roughness. Results showed that implementing grinding reduced the surface roughness of the LPBF AlSi10Mg from 7  $\mu\text{m}$  to 0.6  $\mu\text{m}$ . Further on, applying the magnetic abrasive finishing provided an excellent surface finish free from spheroids, pits, scratches, and pores, and the surface roughness was 0.155  $\mu\text{m}$ . A detailed analysis of post-processing surface treatments can be found in [131,132].

Different from surface treatment, post-heat treatment will effectively reduce residual stresses and alter the microstructure of LPBF HS-Al alloys [133]. The reduction in residual stresses will prevent shape distortion and improve fatigue performance [134]. Heat treatment also modifies the non-equilibrium or metastable microstructure into a stable microstructure, which will affect the part strength and ductility. For example, Wang et al. [135] investigated the effect of T6 aging heat treatment on the mechanical properties of the LPBF-fabricated cast Al alloys. Results showed an increase in elongation by 155%, while the tensile strength decreased by 20%. The change in the resultant mechanical properties of the heat-treated sample was attributed to a change in microstructural features. Before T6 heat treatment, large brittle flakes of Si serve as crack initiation sites, thus reducing the ductility of the samples. During T6 heat treatment, the spheroidization and diffusion of Si precipitates will ensure ductility enhancement. Mehta et al. [44] showed a 42.7% increase in YS and a 22% increase in UTS for T6-aged Zr-modified AA6061. However, the elongation decreases by 49%. This mechanical response for the heat-treated sample was due to the precipitation of the Mg<sub>2</sub>Si and Al<sub>3</sub>Zr phases. Similar observations were also reported for the LPBF-fabricated AA6061 supported by powder-bed preheating, and the resultant mechanical properties are shown in Table 5 [38].

It is important to emphasize that despite the abovementioned effectiveness of post-surface and heat treatment in alleviating defects and improving microstructure [136,137], none of them can thoroughly address the cracking issue in AM of HS-Al alloys. As explained in the cracking section, post-processing techniques cannot change the factors affecting cracking in HS-Al alloys, such as high thermal expansion and contraction, extensive solidification range, and low melt fluidity. Therefore, an effective strategy must be adapted, such as changing the alloy composition, to address cracking in HS-Al alloys.

## 5. Strategies to Improve Printability of HS-Al Alloys—Composition Modification

Compared with process optimization, composition modification is more effective in obtaining a defect-free printing of HS-Al alloys. This paper reviews research progress on modifying existing alloys such as the 2xxx, 6xxx, and 7xxx series and developing new alloys such as Scalmalloy®. Figure 12a summarizes the typical benefits of composition modification to address the cracking problem by decreasing the solidification range, increasing fluidity, and generating equiaxed grain morphology. The alloying elements and additions that have the above benefits include Si, Ti, Sc, Zr, and Ti compounds. Other transitional elements, such as Ta [51], Er [52], and Nb [53], can also act as potential grain refiners in AM of HS-Al alloys.

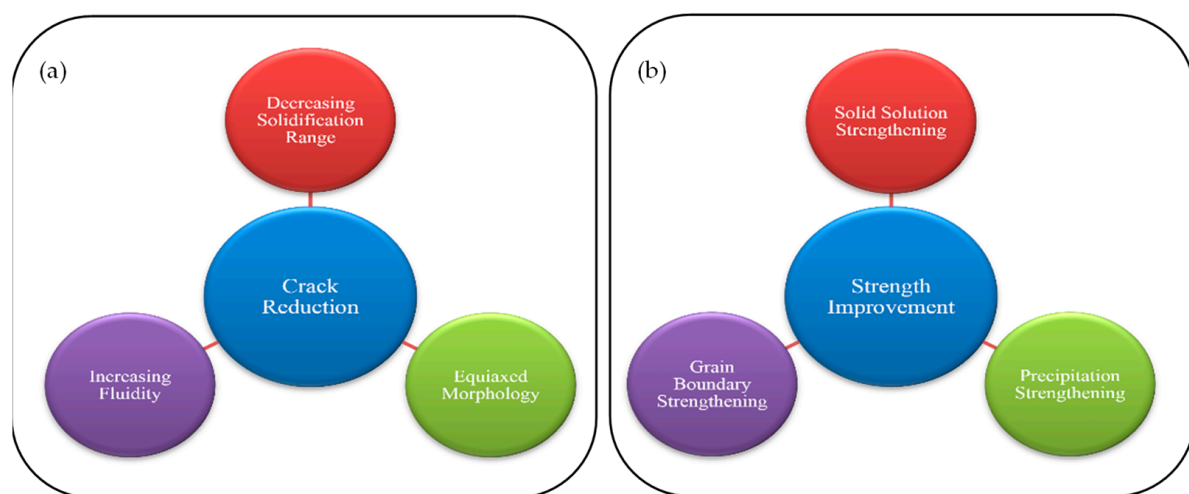


**Figure 12.** Benefits of modification of HS-Al alloys for AM processes: (a) Addressing cracking issues; (b) Improving strength.

The composition modification in HS-Al alloys can also improve strength through the solid solution, grain boundary, and precipitation strengthening mechanisms [60], as shown in Figure 12b. These strengthening phenomena can achieve higher mechanical properties of as-printed samples than the wrought alloys. Table 6 summarizes AM-fabricated compositionally modified HS-Al alloys with various additions and different concentrations, as well as the resultant mechanical properties. The metallurgical effect of representative elements (Si, Ti, Zr, and Sc) on crack alleviation will be discussed in detail.

**Table 6.** Mechanical properties of compositionally modified HS-Al alloys using different alloying additions such as Si, Zr, Ti, Sc, and Ti-based ceramic particles. UTS, YS, STA, and DA represent ultimate tensile strength, yield strength, solution treatment aging, and direct aging, respectively.

Alloying Element	Alloy Series	Manufacturing Condition	YS (MPa)	UTS (MPa)	Elongation (%)	References
5 wt.% Si	7075	As printed	360	537	9.7	[138]
50 wt.% AlSi10Mg	6061	As printed	219.25	353.01	7.3	[26]
4wt.% Si + 2 wt.% TiB <sub>2</sub>	7xxx	As printed	361	445	2.9	[47]
4wt.% Si + 2 wt.% TiB <sub>2</sub>	7xxx	T6-heat treated	453	541	5.3	[47]
1.5 wt.% Ti	2xxx	As printed	293	426	9.1	[139]
1.82 wt.% Ti	7xxx	As printed	-	427	3.9	[140]
2 wt.% Ti/TiN	7xxx	As printed	-	540–550	10	[140]
4 wt.% Ti/TiN	7xxx	As printed	-	595–613	8.8	[140]
6 wt.% Ti/TiN	7xxx	As printed	-	390–402	13.6	[140]
2 wt.% Ti/TiC	6xxx	As printed	-	562	8.8	[54]
3 wt.% TiB <sub>2</sub>	2xxx	As printed	163	284	18.7	[56]
1.3 wt.% Zr	2xxx	As printed	376	441	14.1	[141]
1.3 wt.% Zr	2xxx	STA	402	483	6.9	[141]
1.3 wt.% Zr	2xxx	DA	435	445	7.5	[141]
1.3 wt.% Zr	2xxx	As printed	376 ± 7	441 ± 7	14.1 ± 1.6	[43]
1.3 wt.% Zr	2xxx	T6-heat treated	402 ± 9	483 ± 37	6.9 ± 1.8	[43]
1 wt.% Zr	6xxx	As printed	210	268	26.5	[44]
1 wt.% Zr	6xxx	T6-heat treated	300	327	14	[44]
0.5 wt.% Zr	2xxx	As printed	293	448	11.8	[142]
2 wt.% Zr	2xxx	As printed	464.06 ± 2.04	493.3 ± 10.45	4.76 ± 1.3	[142]
1 wt.% (Sc + Zr)	7xxx	As printed	283	385	18.4	[143]
1 wt.% (Sc + Zr)	7xxx	T6-heat treated	418.3	435.7	11.1	[143]
0.15 wt.% Sc	6xxx	As printed	300	350	31	[121]
1.1 wt.% Sc + 0.42 wt.% Zr	Scalmalloy	As printed	306	334	12.2	[144]
Wrought	2024	T6-heat treated	393	476	10	[34]
Wrought	6061	T6-heat treated	276	310	12	[98]
Wrought	7075	T6-heat treated	480–505	560–572	8–11	[98]

### 5.1. Si

Adding Si has proved to be an effective strategy to reduce cracks in AM of HS-Al alloys. In the case of cast alloys, Si forms a classical eutectic system, rendering high castability and weldability. The formed eutectic will decrease the melting point and solidification range [145]. The DSC analysis indicates a 17 °C decrease in melting point for 4 wt.% Si

added to the AA7075 alloy. Additionally, the formed low melting-point phases  $Mg_2Si$  and  $Al_5Cu_2Mg_8Si_6$  also improve fluidity by providing additional liquid feeding to fill the cracks initiated along the dendritic grain boundary and thus reduce the cracking [138,146].

Compared with Al, Si has a lower coefficient of thermal expansion. Therefore, adding Si will effectively reduce the volumetric change under AM-induced thermal effects and decreases the driving force for crack formation. Moreover, Si can also decrease the cooling rate of AM processes as Si releases four times less latent heat than Al during solidification. As a result, cracking will be alleviated due to the reduced thermal stresses.

Another benefit of Si in increasing resistance to cracking is related to grain refinement [48]. Figure 13 shows the electron backscatter diffraction (EBSD) results of the LPBF-fabricated 7075 alloys with 1–4 wt.% Si additions. The feedstock powders were prepared by mechanical mixing 7075 and Si powders. It can be seen from Figure 13 that the increased Si concentration reduces the quantity of large columnar grains and promotes the formation of small equiaxed grains at melt pool boundaries. The retained columnar grains in the central region of the melt pool are also reduced into short columnar grains. As illustrated in Figure 6, the high-angle grain boundaries of small grains create a larger dihedral angle and shallower liquid-feeding channel, reducing the chance of solidification cracking. Similar grain refinement was also observed in the LPBF-printed 50%-7075 and 50%-AlSi10Mg mixture [60], which was free from cracks and had improved mechanical properties (Table 6). Instead of premixed powders, Otani et al. [138] pre-alloyed 7075 with different contents of Si additions and focused on the influence of Si on printability. The resultant microstructure was characterized by a more uniform composition and grain distribution. Additionally, the required laser energy density to produce dense parts from pre-alloyed powders is less than that of premixed feedstocks. The lower energy density is advantageous for AM of Al alloys since it can reduce the evaporation of low-melting-point elements (e.g., Mg and Zn) and prevent the formation of undesirable precipitates.

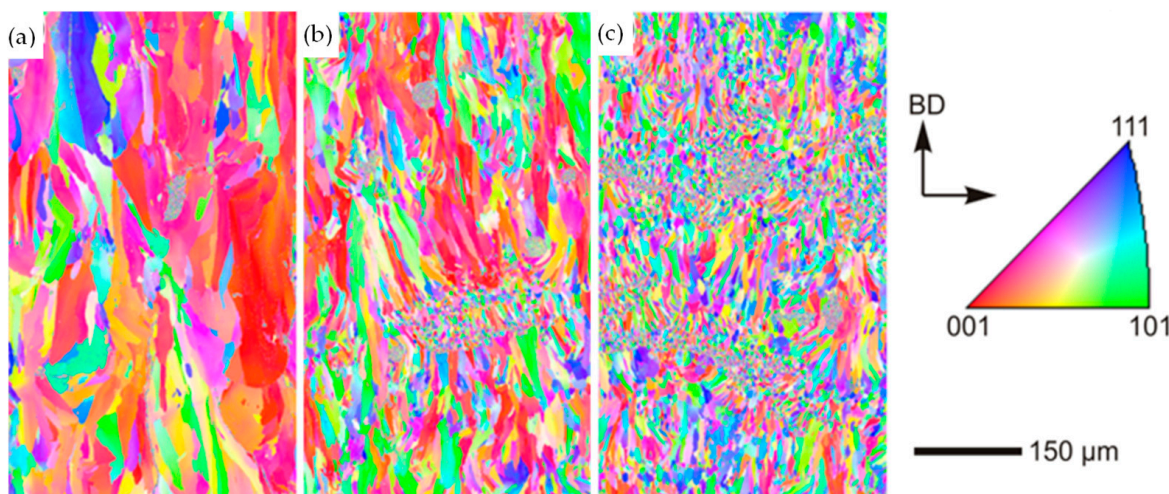


**Figure 13.** EBSD maps of the LPBF-7075 Al alloy with different concentrations of Si additions: (a) 0 wt.%; (b) 2 wt.%; (c) 4 wt.%. Maps are oriented along the build direction. Reproduced with permission from Elsevier [48].

### 5.2. Ti

Ti is another popular grain refiner used in the conventional cast Al alloys. Similarly, it can also be employed in AM of HS-Al alloys. The addition of Ti will lead to the formation of  $Al_3Ti$  precipitates, acting as the heterogeneous nucleation site for the subsequent solidification of the  $\alpha$ -Al matrix and promoting columnar grain to equiaxed transition. It is well known that solute addition is essential in grain refinement as it provides the melt pool with constitutional undercooling, favoring the formation of nucleation sites in the solidification front and reducing the grain size. [147]. As discussed in the previous texts

about the positive effect of grain refinement on reducing defects, the addition of Ti and Ti-based ceramic particles will thus help eliminate cracks and improve the mechanical properties of Al alloy (Table 6). The strengthening effect is achieved by grain refinement provided by  $\text{Al}_3\text{Ti}$  precipitates and can be defined by a parameter known as the growth restriction factor ( $Q$ ). This factor determines the final grain size ( $d$ ) of the fabricated alloy as  $d = k \sqrt[3]{1/Q}$  [148]. The higher  $Q$  value of Ti demonstrates its capability of restricting grain growth. A slight lattice mismatch between the matrix material and nuclei would ensure a coherent/semi-coherent interface by minimizing the interfacial energy [149]. While more Ti additions tend to form more nucleation sites, the excessive  $\text{Al}_3\text{Ti}$  precipitates will deteriorate ductility. Based on the thermodynamic calculation, 1.5 wt.% Ti addition is optimum to achieve an effective grain refinement effect without brittleness transition.

Like Ti particles, Ti-based ceramic particles such as  $\text{TiC}$ ,  $\text{TiN}$ , and  $\text{TiB}_2$  can also be added to high-strength Al alloys to enhance strength and solidification behaviors during AM processes [55,56,150]. The study by Li et al. [54] illustrated that the inclusion of ceramic particles enhanced the mechanical properties of the Al matrix by forming metal matrix composites. However, the interfacial bonding between the ceramic particles and fused metal depends upon the wettability of particles and surface tension. Using mixed grain refiners (Ti and  $\text{TiN}$ ) can limit the weak bond as Ti provides sufficient wettability to ceramic particles by introducing intense Marangoni convection and also contributes to resisting the agglomeration of ceramic particles, thereby increasing the nucleation efficiency [140]. The obtained micrographs comparing the grain refinement effects among Ti,  $\text{TiN}$ , and Ti/ $\text{TiN}$  mixture for AM of AA7050 are shown in Figure 14.

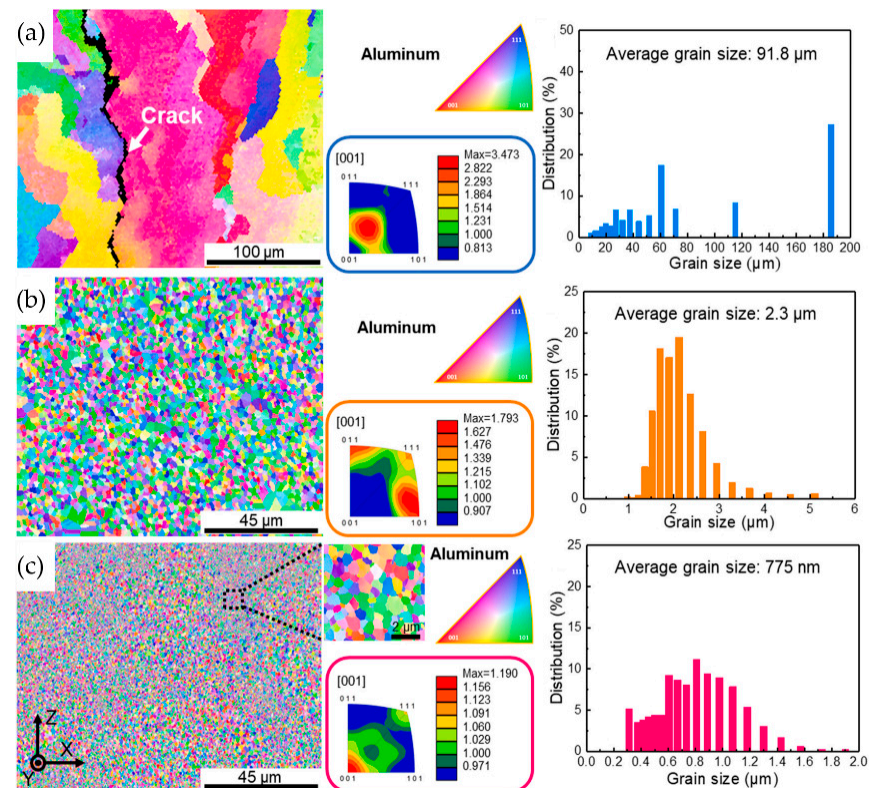


**Figure 14.** EBSD maps of the LPBF-printed AA7075 Al alloy: (a) Pure AA7050; (b) 7050-1.82 wt.%Ti; (c) 7050-2 wt%Ti/TiN. Reproduced with permission from Elsevier [140].

### 5.3. Zr

The addition of Zr also improves the AM processability of HS-Al alloys. The addition of 1wt.% Zr and a heated build plate at 100 °C have significantly reduced porosity and cracks for AM AA-6061 [44]. Adding 2 wt.% Zr to the Al-Cu-Mg alloy reduced the solidification range and produced higher density and a larger processing window [142].

DSC analysis shown in Figure 15 confirmed these observations, where the solidification temperature range for 2 wt.% Zr was minimum, inhibiting the formation of a large dendritic structure and suppressing the chances of forming solidification cracks. Moreover, the thermal conductivity decreases with an increase in Zr content. Lower thermal conductivity will stabilize the melt pool dynamics due to low Marangoni force and improve the liquid flowability because of the decreased viscosity with regards to the mechanical properties of Zr-modified alloy. 2wt.% Zr addition showed the highest yield strength (YS) and ultimate tensile strength (UTS) but with the lowest ductility [142] (Table 6).

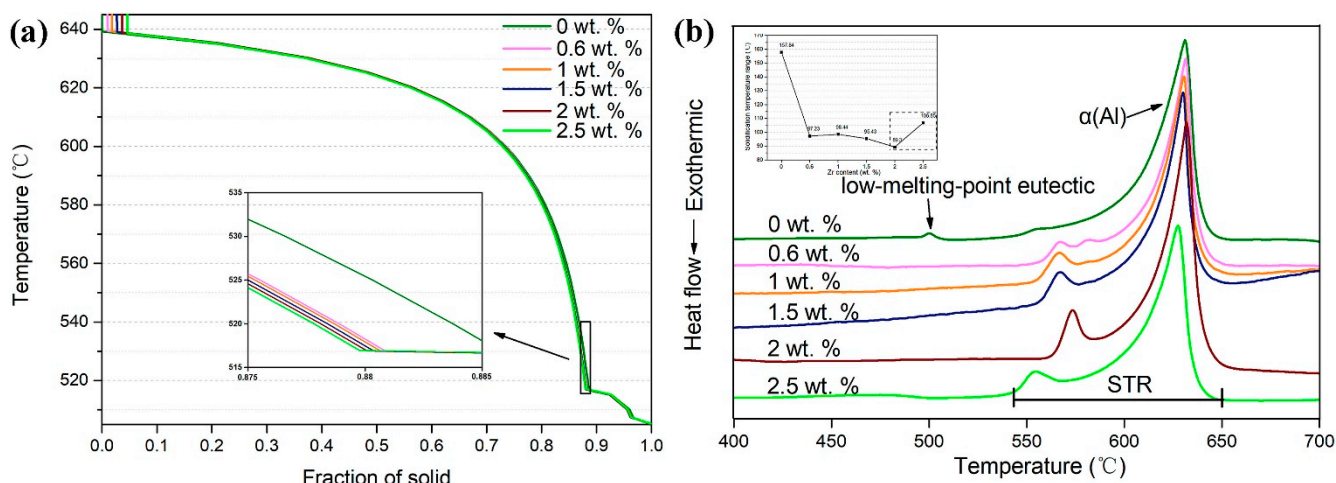


**Figure 15.** (a) Scheil-Gulliver simulation and (b) DSC analysis of the solidification temperature range (STR) for different concentrations of Zr additions. Reproduced with permission from Elsevier [142].

Additionally, Zr has a lower  $Q$  value than Ti, which indicates a less effective restriction on grain growth [61]. However, the lattice mismatch between the formed  $\text{Al}_3\text{Zr}$  and  $\alpha$ -Al is smaller than that between  $\text{Al}_3\text{Ti}$  and  $\alpha$ -Al, favoring a coherent/semi-coherent interface between precipitates and matrix [149]. The positive effect of  $\text{Al}_3\text{Zr}$  in grain refinement has been discussed by Wang et al. [43], where a heterogeneous grain structure was formed by adding Zr to the AM of Al-Cu-Mg alloy. The equiaxed structure is visible at the melt pool boundaries, while the columnar structure is still retained near the center of the melt pool. Based on the constitutional undercooling and time-dependent nucleation theory, it is postulated that the high intensity of nucleating agents  $\text{Al}_3\text{Zr}$  at the fusion zone is responsible for the equiaxed morphology at melt pool boundaries [151]. The precipitation of metastable  $\text{Al}_3\text{Zr}$  precipitates is associated with AM's high cooling rate. However, in the inner region of the melt pool, no precipitation of primary  $\text{Al}_3\text{Zr}$  precipitates occurs due to a lower cooling rate. The shorter columnar grains in Zr-modified alloy are formed because a fine-equiaxed structure of the previous fused layer will inhibit epitaxial grain growth during subsequent deposition. Additionally, Zr has a high oxygen affinity and is easy to form  $\text{ZrO}_2$ , contributing to heterogeneous nucleation sites and promoting grain refinement [152].

Similar to  $\text{Al}_3\text{Zr}$ , adding yttria-stabilized zirconia (YSZ) and  $\text{ZrH}_2$  particles to an Al powder also showed tremendous benefits in crack reduction [153,154]. However, special powder pre-processing is required for these compounds; for example, YSZ particles should be first electrostatically stuck to Al powder to ensure uniform distribution and prevent agglomeration. A mixing duration of 10 h to 20 h was required to provide a good grip between YSZ particles and Al powders.

#### 5.4. Sc

Adding Sc to cast and HS-Al alloys during conventional manufacturing has been adopted for a long time. It is a rare earth element and has proved to be one of the most effective grain refiners when added to Al in an optimum quantity. Qbau et al. [121] also

claimed that Sc helped improve the stability and powder flowability of Sc-modified AA6061 alloy. The improved powder flowability is attributed to the presence of fewer satellites, thus requiring less energy in the rheological test compared with unmodified alloy. Additionally, the formation of  $\text{Al}_3\text{Sc}$  also effectively reduces the hot cracking susceptibility and provides grain refinement. During AM processing of Al-Sc alloys, a supersaturated Al-Sc solid solution with minor coherent  $\text{Al}_3\text{Sc}$  precipitates may be formed due to the high cooling rate of metal AM processes. These  $\text{Al}_3\text{Sc}$  precipitates will serve as heterogeneous nuclei and reduce the grain size. Based on this theory, the airbus group has developed Scalmalloy<sup>®</sup>, which exhibits excellent ductility and tensile strength due to precipitate strengthening (Table 6). In several studies, Zr was also added along with Sc since both elements show remarkable effects in grain refinement, and Zr helps stabilize and intensify the effects of Sc by contributing to columnar to equiaxed transition [155]. Zhou et al. [57] showed that the formation of equiaxed grains is process-dependent, especially by using higher energy density, which plays a crucial role in distributing the Sc and Zr nanoparticles within the melt pool. An even distribution of added elements was achieved for higher energy density due to the fluid flow associated with the Marangoni convection [156]. Therefore, the as-printed Sc-modified Al alloy can have more equiaxed grains with high energy density, as shown in Figure 16.

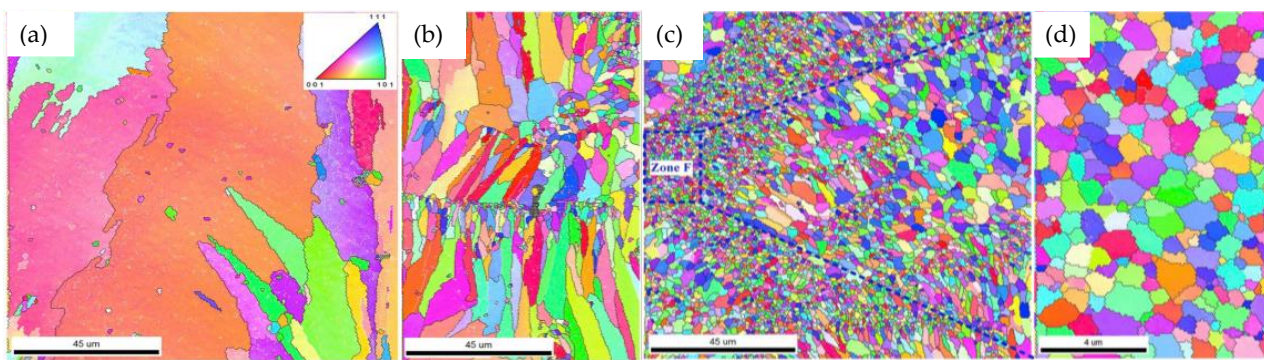


**Figure 16.** EBSD orientation maps of Sc- and Zr-modified 7075 alloy at different energy densities: (a)  $44 \text{ J/mm}^3$ ; (b)  $167 \text{ J/mm}^3$ ; (c)  $375 \text{ J/mm}^3$ ; (d) magnified zone. Reproduced with permission from Elsevier [156].

## 6. Conclusions

In this review paper, the metallurgical challenges and effective strategies adapted to improve the printability of HS-Al alloys are discussed in detail. The primary findings are summarized below:

1. Metal AM of HS-Al alloys suffers from poor printability that features cracking and porosity due to the extensive solidification range, high thermal conductivity, significant thermal expansion, low absorptivity, poor fluidity, and oxide formation in the melt pool.
2. Ideal material candidates for metal AM should have good weldability, castability, and heat treatability; however, these criteria are necessary but insufficient to guarantee good printability.
3. Optimizing process conditions through improving AM parameters and incorporating hybrid processes such as preheating, remelting, and laser beam oscillation can reduce porosity significantly but fail to eliminate cracks thoroughly.
4. Composition modification is the most effective strategy to address cracking. Si primarily improves the melt pool fluidity and reduces the solidification range by forming a eutectic mixture. Ti, Zr, Sc, Ta, Er, Nb, and their compounds provide heterogeneous nucleation agents such as  $\text{Al}_3\text{Ti}$ ,  $\text{Al}_3\text{Zr}$ , and  $\text{Al}_3\text{Sc}$ , which refine grain structure by transforming columnar grain into equiaxed morphology, suppressing the crack formation and strengthening the Al matrix by forming precipitate reinforcements.

## 7. Outlook

Numerous research efforts have been carried out on the challenges and strategies regarding AM of HS-Al alloys. These attempts are focused on AM technologies and material innovations. Therefore, it is necessary to provide confinement and direction for future research based on the current breakthroughs reviewed in this work.

Regarding AM technologies, optimization of AM parameters has little effect on the complete removal of cracks due to the inherent incompatible thermal and metallurgical properties of HS-Al alloys with metal AM. Another attempt is to develop hybrid AM processes by incorporating favorable secondary processes or energy sources to help inhibit crack formation and reduce porosity. For instance, preheating the powder bed at a high temperature of around 500–550 °C will decrease the cooling rate and thermal stresses, which will reduce crack formation's driving force. However, the research on hybrid AM processes is still limited. Since the processing window is narrow, in-process monitoring, and quantitative studies will help control and optimize the process.

At present, composition modification is an effective strategy to terminate cracking in AM of HS-Al alloys. Many suitable elements can be added; however, they should satisfy the following characteristics: (i) ability to reduce solidification range, (ii) capability to form precipitates with Al, (iii) capacity to improve mechanical properties, and (iv) potential to reduce cost. Si, Zr, Ti, and Sc are reviewed in this work, and their abilities to resist cracking are discussed in detail. All these elements or their precipitates provide heterogeneous nucleation sites and promote grain refinement. However, Sc is a costly rare earth element. From the metallurgical viewpoint, the potential nucleating agent should have a high growth restriction factor ( $Q$ ) that favors the formation of equiaxed grains. Ti has a higher  $Q$  value than Zr, and thus it is more effective in suppressing cracks. Compared with Si and Ti, Si can effectively reduce the solidification range but fails to form precipitate reinforcements. Therefore, Ti is the best addition to modify HS-Al compositions. Instead of in-situ alloying, ex-situ introduction of inclusions such as TiC, TiN, and SiC can also be used as crack suppressants and mechanical reinforcements. It is also important to highlight that composition modification belongs to new material development. Mechanical properties of composition-modified HS-Al parts should be thoroughly evaluated compared to non-modified counterparts.

Since process optimization and composition modification produce extensive data, machine learning (ML) algorithms have been intensively employed to establish the composition-process-microstructure-property relationship [157], which has significantly reduced the overall experimental cost [158]. Commonly used ML models in AM processes include K-means clustering (KNN) [159], linear support vector machine (SVM) [160], gaussian process (GP) [161], random forest (RF) [162], artificial neural network (ANN) [163], and convolutional neural network (CNN) [164]. The selection of these ML models depends on specific requirements such as accuracy, efficiency, and cost. Regarding process control and optimal parameter prediction, Liu et al. [161] developed a GP model for optimizing the processing window for the LPBF of Al alloys. The model provided a much larger processing window with an almost wholly dense part and an excellent combination of strength and ductility compared with other ML techniques. For property prediction based on microstructural features, Muhammad et al. [163] successfully developed an ANN model to predict local strains, plastic anisotropy, and failure during tensile deformation for AlSi10Mg while taking the experimental input data from digital image correlation and X-ray computed tomography scans. It is worth noting that data quality and quantity significantly affect the accuracy of ML prediction. For example, using an experimental microstructure dataset to train an ML model, the 2D material characterization will be less representative than the 3D material design space. Using only AM parameters as inputs cannot predict cracking tendency accurately, as cracking also depends on the solidification thermodynamics in AM of HS-Al alloys [138]. Therefore, it is necessary to understand the critical physics required to accurately predict the cracking behavior by creating a new physics-augmented ML process optimization and design platform that can be trained with reduced experimental data.

**Author Contributions:** Conceptualization, S.L.; methodology, S.L.; validation, S.D.; formal analysis, S.D.; investigation, S.D.; data curation, S.D.; writing—original draft preparation, S.D.; writing—review and editing, S.L.; supervision, S.L.; project administration, S.L.; funding acquisition, S.L. All authors have read and agreed to the published version of the manuscript.

**Funding:** This research was sponsored by the DEVCOM Army Research Laboratory and was accomplished under Cooperative Agreement Number W911NF2020237. The views and conclusions contained in this document are those of the authors and should not be interpreted as representing the official policies, either expressed or implied, of the Army Research Laboratory or the U.S. Government. The U.S. Government is authorized to reproduce and distribute reprints for Government purposes, notwithstanding any copyright notation herein.

**Data Availability Statement:** Not applicable.

**Acknowledgments:** The second author would also like to thank William Michael Riechers for his assistance in literature reviews.

**Conflicts of Interest:** The authors declare no conflict of interest.

## References

- Das, S.K.; Green, J.A.S.; Kaufman, J.G. The development of recycle-friendly automotive aluminum alloys. *JOM* **2007**, *59*, 47–51. [[CrossRef](#)]
- Mahfoud, M.; Emadi, D. Aluminum recycling-Challenges and opportunities. *Proc. Adv. Mater. Res.* **2010**, *83*, 571–578. [[CrossRef](#)]
- Starke, E.A.; Staley, J.T. Application of modern aluminum alloys to aircraft. *Prog. Aerosp. Sci.* **1996**, *32*, 131–172. [[CrossRef](#)]
- Kermanidis, A.T. Aircraft Aluminum Alloys: Applications and Future Trends. In *Revolutionizing Aircraft Materials and Processes*; Springer: Cham, Switzerland, 2020.
- Nakata, M.; Kitahara, Y.; Haguchi, H. Trends in aluminum alloy casting for aircraft parts. *Res. Dev.-Kobe* **2005**, *55*, 87.
- Sun, H.T.; Wang, J.; Shen, G.Z.; Hu, P. Application of warm forming aluminum alloy parts for automotive body based on impact. *Int. J. Automot. Technol.* **2013**, *14*, 605–610. [[CrossRef](#)]
- Yang, T.; Liu, T.; Liao, W.; MacDonald, E.; Wei, H.; Zhang, C.; Chen, X.; Zhang, K. Laser powder bed fusion of AlSi10Mg: Influence of energy intensities on spatter and porosity evolution, microstructure and mechanical properties. *J. Alloys Compd.* **2020**, *849*, 156300. [[CrossRef](#)]
- Moghimian, P.; Poirié, T.; Habibnejad-Korayem, M.; Zavala, J.A.; Kroeger, J.; Marion, F.; Larouche, F. Metal powders in additive manufacturing: A review on reusability and recyclability of common titanium, nickel and aluminum alloys. *Addit. Manuf.* **2021**, *43*, 102017. [[CrossRef](#)]
- Yao, X.; Moon, S.K.; Bi, G.; Wei, J. A multi-material part design framework in additive manufacturing. *Int. J. Adv. Manuf. Technol.* **2018**, *99*, 2111–2119. [[CrossRef](#)]
- Leicher, M.; Kamper, S.; Treutler, K.; Wesling, V. Multi-material design in additive manufacturing—Feasibility validation. *Weld. World* **2020**, *64*, 1341–1347. [[CrossRef](#)]
- Haghdadi, N.; Laleh, M.; Moyle, M.; Primig, S. Additive manufacturing of steels: A review of achievements and challenges. *J. Mater. Sci.* **2021**, *56*, 64–107. [[CrossRef](#)]
- Agrawal, R.; Vinodh, S. State of art review on sustainable additive manufacturing. *Rapid Prototyp. J.* **2019**, *25*, 1045–1060. [[CrossRef](#)]
- Liu, S.; Shin, Y.C. Additive manufacturing of Ti6Al4V alloy: A review. *Mater. Des.* **2019**, *164*, 107552. [[CrossRef](#)]
- Marattukalam, J.J.; Karlsson, D.; Pacheco, V.; Beran, P.; Wiklund, U.; Jansson, U.; Hjörvarsson, B.; Sahlberg, M. The effect of laser scanning strategies on texture, mechanical properties, and site-specific grain orientation in selective laser melted 316L SS. *Mater. Des.* **2020**, *193*, 108852. [[CrossRef](#)]
- Salman, O.O.; Brenne, F.; Niendorf, T.; Eckert, J.; Prashanth, K.G.; He, T.; Scudino, S. Impact of the scanning strategy on the mechanical behavior of 316L steel synthesized by selective laser melting. *J. Manuf. Process.* **2019**, *45*, 255–261. [[CrossRef](#)]
- Bajaj, P.; Hariharan, A.; Kini, A.; Kürnsteiner, P.; Raabe, D.; Jägle, E.A. Steels in additive manufacturing: A review of their microstructure and properties. *Mater. Sci. Eng. A* **2020**, *772*, 138633. [[CrossRef](#)]
- Babu, S.S.; Raghavan, N.; Raplee, J.; Foster, S.J.; Frederick, C.; Haines, M.; Dinwiddie, R.; Kirka, M.K.; Plotkowski, A.; Lee, Y.; et al. Additive Manufacturing of Nickel Superalloys: Opportunities for Innovation and Challenges Related to Qualification. *Metall. Mater. Trans. A Phys. Metall. Mater. Sci.* **2018**, *49*, 3764–3780. [[CrossRef](#)]
- Li, Y.; Liang, X.; Yu, Y.; Wang, D.; Lin, F. Review on Additive Manufacturing of Single-Crystal Nickel-based Superalloys. *Chin. J. Mech. Eng. Addit. Manuf. Front.* **2022**, *1*, 100019. [[CrossRef](#)]
- Liu, S.; Grohol, C.M.; Shin, Y.C. High throughput synthesis of CoCrFeNiTi high entropy alloys via directed energy deposition. *J. Alloys Compd.* **2022**, *916*, 165469. [[CrossRef](#)]
- Klocke, F.; Arntz, K.; Teli, M.; Winands, K.; Wegener, M.; Oliari, S. State-of-the-art Laser Additive Manufacturing for Hot-work Tool Steels. *Procedia CIRP* **2017**, *63*, 58–63. [[CrossRef](#)]

21. Mauduit, A.; Pillot, S.; Gransac, H. Study of the suitability of aluminum alloys for additive manufacturing by laser powder-bed fusion. *UPB Sci. Bull. Ser. B Chem. Mater. Sci.* **2017**, *79*, 219–238.
22. Reschetnik, W.; Brüggemann, J.P.; Aydinöz, M.E.; Grydin, O.; Hoyer, K.P.; Kullmer, G.; Richard, H.A. Fatigue crack growth behavior and mechanical properties of additively processed en AW-7075 aluminium alloy. *Procedia Struct. Integr.* **2016**, *2*, 3040–3048. [[CrossRef](#)]
23. Brice, C.A.; Tayon, W.A.; Newman, J.A.; Kral, M.V.; Bishop, C.; Sokolova, A. Effect of compositional changes on microstructure in additively manufactured aluminum alloy 2139. *Mater. Charact.* **2018**, *143*, 50–58. [[CrossRef](#)]
24. Brice, C.; Shenoy, R.; Kral, M.; Buchannan, K. Precipitation behavior of aluminum alloy 2139 fabricated using additive manufacturing. *Mater. Sci. Eng. A* **2015**, *648*, 9–14. [[CrossRef](#)]
25. Kimura, T.; Nakamoto, T. Microstructures and mechanical properties of A356 (AlSi7Mg0.3) aluminum alloy fabricated by selective laser melting. *Mater. Des.* **2016**, *89*, 1294–1301. [[CrossRef](#)]
26. Bradford, R.L.; Cao, L.; Klosterman, D.; Herman, F.; Forman, L.; Browning, C. A metal–metal powder formulation approach for laser additive manufacturing of difficult-to-print high-strength aluminum alloys. *Mater. Lett.* **2021**, *300*, 130113. [[CrossRef](#)]
27. McDonald, S.D.; Nogita, K.; Dahle, A.K. Eutectic nucleation in Al-Si alloys. *Acta Mater.* **2004**, *52*, 4273–4280. [[CrossRef](#)]
28. Aboulkhair, N.T.; Simonelli, M.; Parry, L.; Ashcroft, I.; Tuck, C.; Hague, R. 3D printing of Aluminium alloys: Additive Manufacturing of Aluminium alloys using selective laser melting. *Prog. Mater. Sci.* **2019**, *106*, 100578. [[CrossRef](#)]
29. Rooy, E.L. Introduction to Aluminum and Aluminum Alloys. In *Properties and Selection: Nonferrous Alloys and Special-Purpose Materials*; ASM International: Almere, The Netherlands, 2018.
30. Kaufmann, N.; Imran, M.; Wischeropp, T.M.; Emmelmann, C.; Siddique, S.; Walther, F. Influence of process parameters on the quality of aluminium alloy en AW 7075 using Selective Laser Melting (SLM). *Phys. Procedia* **2016**, *83*, 918–926. [[CrossRef](#)]
31. Pekok, M.A.; Setchi, R.; Ryan, M.; Han, Q.; Gu, D. Effect of process parameters on the microstructure and mechanical properties of AA2024 fabricated using selective laser melting. *Int. J. Adv. Manuf. Technol.* **2021**, *112*, 175–192. [[CrossRef](#)]
32. Oko, O.E.; Mbakaan, C.; Barki, E. Experimental investigation of the effect of processing parameters on densification, microstructure and hardness of selective laser melted 7075 aluminium alloy. *Mater. Res. Express* **2020**, *7*, 036512. [[CrossRef](#)]
33. Maamoun, A.H.; Xue, Y.F.; Elbestawi, M.A.; Veldhuis, S.C. Effect of selective laser melting process parameters on the quality of al alloy parts: Powder characterization, density, surface roughness, and dimensional accuracy. *Materials* **2018**, *11*, 2343. [[CrossRef](#)] [[PubMed](#)]
34. Zhang, H.; Zhu, H.; Qi, T.; Hu, Z.; Zeng, X. Selective laser melting of high strength Al-Cu-Mg alloys: Processing, microstructure and mechanical properties. *Mater. Sci. Eng. A* **2016**, *656*, 47–54. [[CrossRef](#)]
35. Giganto, S.; Zapico, P.; Castro-Sastre, M.Á.; Martínez-Pellitero, S.; Leo, P.; Perulli, P. Influence of the scanning strategy parameters upon the quality of the SLM parts. *Proc. Procedia Manuf.* **2019**, *41*, 698–705. [[CrossRef](#)]
36. Koutny, D.; Palousek, D.; Pantalejev, L.; Hoeller, C.; Pichler, R.; Tesicky, L.; Kaiser, J. Influence of scanning strategies on processing of aluminum alloy EN AW 2618 using selective laser melting. *Materials* **2018**, *11*, 298. [[CrossRef](#)] [[PubMed](#)]
37. Yasa, E.; Kruth, J.P. Microstructural investigation of selective laser melting 316 L stainless steel parts exposed to laser re-melting. *Procedia Eng.* **2011**, *19*, 389–395. [[CrossRef](#)]
38. Uddin, S.Z.; Murr, L.E.; Terrazas, C.A.; Morton, P.; Roberson, D.A.; Wicker, R.B. Processing and characterization of crack-free aluminum 6061 using high-temperature heating in laser powder bed fusion additive manufacturing. *Addit. Manuf.* **2018**, *22*, 405–415. [[CrossRef](#)]
39. Wu, D.; Liu, D.; Niu, F.; Miao, Q.; Zhao, K.; Tang, B.; Bi, G.; Ma, G. Al–Cu alloy fabricated by novel laser-tungsten inert gas hybrid additive manufacturing. *Addit. Manuf.* **2020**, *32*, 100954. [[CrossRef](#)]
40. Liu, D.; Wu, D.; Wang, R.; Shi, J.; Niu, F.; Ma, G. Formation mechanism of Al-Zn-Mg-Cu alloy fabricated by laser-arc hybrid additive manufacturing: Microstructure evaluation and mechanical properties. *Addit. Manuf.* **2022**, *50*, 102554. [[CrossRef](#)]
41. Skalicky, P.; Koutny, D.; Pantalejev, L.; Palousek, D. Processing of Aluminum Alloy En Aw 7075 Using Selective Laser Melting: Initial Study. In Proceedings of the 58th International Conference of Machine Design Departments (ICMD 2017), Prague, Czech Republic, 6–8 September 2017.
42. Roberts, C.E.; Bourell, D.; Watt, T.; Cohen, J. A novel processing approach for additive manufacturing of commercial aluminum alloys. *Phys. Procedia* **2016**, *83*, 909–917. [[CrossRef](#)]
43. Wang, Y.; Lin, X.; Kang, N.; Wang, Z.; Wang, Q.; Liu, Y.; Huang, W. Laser powder bed fusion of Zr-modified Al–Cu–Mg alloy: Crack-inhibiting, grain refinement, and mechanical properties. *Mater. Sci. Eng. A* **2022**, *838*, 142618. [[CrossRef](#)]
44. Mehta, A.; Zhou, L.; Huynh, T.; Park, S.; Hyer, H.; Song, S.; Bai, Y.; Imholte, D.D.; Woolstenhulme, N.E.; Wachs, D.M.; et al. Additive manufacturing and mechanical properties of the dense and crack free Zr-modified aluminum alloy 6061 fabricated by the laser-powder bed fusion. *Addit. Manuf.* **2021**, *41*, 101966. [[CrossRef](#)]
45. Tian, S.; Li, J.; Zhang, J.; Wulabieke, Z.; Lv, D. Effect of Zr and Sc on microstructure and properties of 7136 aluminum alloy. *J. Mater. Res. Technol.* **2019**, *8*, 4130–4140. [[CrossRef](#)]
46. Yang, K.V.; Shi, Y.; Palm, F.; Wu, X.; Rometsch, P. Columnar to equiaxed transition in Al-Mg-(Sc)-Zr alloys produced by selective laser melting. *Scr. Mater.* **2018**, *145*, 113–117. [[CrossRef](#)]
47. Zhou, S.Y.; Su, Y.; Wang, H.; Enz, J.; Ebel, T.; Yan, M. Selective laser melting additive manufacturing of 7xxx series Al-Zn-Mg-Cu alloy: Cracking elimination by co-incorporation of Si and TiB<sub>2</sub>. *Addit. Manuf.* **2020**, *36*, 101458. [[CrossRef](#)]

48. Montero Sistiaga, M.L.; Mertens, R.; Vrancken, B.; Wang, X.; Van Hooreweder, B.; Kruth, J.P.; Van Humbeeck, J. Changing the alloy composition of Al7075 for better processability by selective laser melting. *J. Mater. Process. Technol.* **2016**, *238*, 437–445. [CrossRef]
49. Liu, X.; Liu, Y.; Zhou, Z.; Zhan, Q. Enhanced strength and ductility in Al-Zn-Mg-Cu alloys fabricated by laser powder bed fusion using a synergistic grain-refining strategy. *J. Mater. Sci. Technol.* **2022**, *124*, 41–52. [CrossRef]
50. Tan, Q.; Zhang, J.; Sun, Q.; Fan, Z.; Li, G.; Yin, Y.; Liu, Y.; Zhang, M.X. Inoculation treatment of an additively manufactured 2024 aluminum alloy with titanium nanoparticles. *Acta Mater.* **2020**, *196*, 1–16. [CrossRef]
51. Martin, J.H.; Yahata, B.; Mayer, J.; Mone, R.; Stonkevitch, E.; Miller, J.; O'Masta, M.R.; Schaedler, T.; Hundley, J.; Callahan, P.; et al. Grain refinement mechanisms in additively manufactured nano-functionalized aluminum. *Acta Mater.* **2020**, *200*, 1022–1037. [CrossRef]
52. Guo, Y.; Wei, W.; Shi, W.; Zhang, B.; Zhou, X.; Wen, S.; Wu, X.; Gao, K.; Rong, L.; Huang, H.; et al. Effect of Er and Zr additions and aging treatment on grain refinement of aluminum alloy fabricated by laser powder bed fusion. *J. Alloys Compd.* **2022**, *912*, 165237. [CrossRef]
53. Wang, Z.; Wang, X.; Chen, X.; Qiu, C. Complete columnar-to-equiaxed transition and significant grain refinement in an aluminium alloy by adding Nb particles through laser powder bed fusion. *Addit. Manuf.* **2022**, *51*, 102615. [CrossRef]
54. Xinwei, L.; Shi, S.; Shuang, H.; Xiaogang, H.; Qiang, Z.; Hongxing, L.; Wenwu, L.; Yusheng, S.; Hui, D. Microstructure, solidification behavior and mechanical properties of Al-Si-Mg-Ti/TiC fabricated by selective laser melting. *Addit. Manuf.* **2020**, *34*, 101326. [CrossRef]
55. Xi, L.; Guo, S.; Gu, D.; Guo, M.; Lin, K. Microstructure development, tribological property and underlying mechanism of laser additive manufactured submicro-TiB<sub>2</sub> reinforced Al-based composites. *J. Alloys Compd.* **2020**, *819*, 152980. [CrossRef]
56. Wen, X.; Wang, Q.; Mu, Q.; Kang, N.; Sui, S.; Yang, H.; Lin, X.; Huang, W. Laser solid forming additive manufacturing TiB<sub>2</sub> reinforced 2024Al composite: Microstructure and mechanical properties. *Mater. Sci. Eng. A* **2019**, *745*, 319–325. [CrossRef]
57. Zhou, L.; Hyer, H.; Thapliyal, S.; Mishra, R.S.; McWilliams, B.; Cho, K.; Sohn, Y. Process-Dependent Composition, Microstructure, and Printability of Al-Zn-Mg and Al-Zn-Mg-Sc-Zr Alloys Manufactured by Laser Powder Bed Fusion. *Metall. Mater. Trans. A Phys. Metall. Mater. Sci.* **2020**, *51*, 3215–3227. [CrossRef]
58. Zhang, J.; Song, B.; Wei, Q.; Bourell, D.; Shi, Y. A review of selective laser melting of aluminum alloys: Processing, microstructure, property and developing trends. *J. Mater. Sci. Technol.* **2019**, *35*, 270–284. [CrossRef]
59. Galy, C.; Le Guen, E.; Lacoste, E.; Arvieu, C. Main defects observed in aluminum alloy parts produced by SLM: From causes to consequences. *Addit. Manuf.* **2018**, *22*, 165–175. [CrossRef]
60. Aversa, A.; Marchese, G.; Saboori, A.; Bassini, E.; Manfredi, D.; Biamino, S.; Ugues, D.; Fino, P.; Lombardi, M. New aluminum alloys specifically designed for laser powder bed fusion: A review. *Materials* **2019**, *12*, 1007. [CrossRef]
61. Kotadia, H.R.; Gibbons, G.; Das, A.; Howes, P.D. A review of Laser Powder Bed Fusion Additive Manufacturing of aluminium alloys: Microstructure and properties. *Addit. Manuf.* **2021**, *46*, 102155. [CrossRef]
62. Altiparmak, S.C.; Yardley, V.A.; Shi, Z.; Lin, J. Challenges in additive manufacturing of high-strength aluminium alloys and current developments in hybrid additive manufacturing. *Int. J. Light. Mater. Manuf.* **2021**, *4*, 246–261. [CrossRef]
63. Asnafi, N. Metal additive manufacturing—State of the art 2020. *Metals* **2021**, *11*, 867. [CrossRef]
64. Davis, J.R. *Aluminum and Aluminum Alloys, ASM Specialty Handbook*; ASM International: Almere, The Netherlands, 1993.
65. Luo, A.A. Recent advances in light metals and manufacturing for automotive applications. *CIM J.* **2021**, *13*, 79–87. [CrossRef]
66. Boillat, R.; Isanaka, S.P.; Liou, F. The effect of nanostructures in aluminum alloys processed using additive manufacturing on microstructural evolution and mechanical performance behavior. *Crystals* **2021**, *11*, 524. [CrossRef]
67. Nie, J.F.; Muddle, B.C. Microstructural design of high-strength aluminum alloys. *J. Phase Equilibria* **1998**, *19*, 217, 1251–1256. [CrossRef]
68. Zhang, X.; Deng, Y.; Zhang, Y. Development of high strength aluminum alloys and processing techniques for the materials. *Jinshu Xuebao/Acta Metall. Sin.* **2015**, *51*, 257–271. [CrossRef]
69. METAL Supermarkets 7 Things to Consider When Choosing an Aluminum Grade. 2015. Available online: <https://www.metalsupermarkets.com/7-things-consider-choosing-aluminum-grade/> (accessed on 19 January 2020).
70. Oliveira, J.P.; LaLonde, A.D.; Ma, J. Processing parameters in laser powder bed fusion metal additive manufacturing. *Mater. Des.* **2020**, *193*, 108762. [CrossRef]
71. Mosallanejad, M.H.; Niroumand, B.; Aversa, A.; Saboori, A. In-Situ alloying in laser-based additive manufacturing processes: A critical review. *J. Alloys Compd.* **2021**, *872*, 159567. [CrossRef]
72. Dass, A.; Moridi, A. State of the art in directed energy deposition: From additive manufacturing to materials design. *Coatings* **2019**, *9*, 418. [CrossRef]
73. Gokuldoss, P.K.; Kolla, S.; Eckert, J. Additive manufacturing processes: Selective laser melting, electron beam melting and binder jetting-selection guidelines. *Materials* **2017**, *10*, 672. [CrossRef]
74. Campbell, I.; Bourell, D.; Gibson, I. Additive manufacturing: Rapid prototyping comes of age. *Rapid Prototyp. J.* **2012**, *18*, 255–258. [CrossRef]
75. Xia, C.; Pan, Z.; Polden, J.; Li, H.; Xu, Y.; Chen, S.; Zhang, Y. A review on wire arc additive manufacturing: Monitoring, control and a framework of automated system. *J. Manuf. Syst.* **2020**, *57*, 31–45. [CrossRef]
76. Panwisawas, C.; Tang, Y.T.; Reed, R.C. Metal 3D printing as a disruptive technology for superalloys. *Nat. Commun.* **2020**, *11*, 2327. [CrossRef]

77. Qiu, C.; Kindi, M.A.; Aladawi, A.S.; Hatmi, I. Al a comprehensive study on microstructure and tensile behaviour of a selectively laser melted stainless steel. *Sci. Rep.* **2018**, *8*, 7785. [[CrossRef](#)]
78. Sun, Z.; Tan, X.; Tor, S.B.; Yeong, W.Y. Selective laser melting of stainless steel 316L with low porosity and high build rates. *Mater. Des.* **2016**, *104*, 197–204. [[CrossRef](#)]
79. Vikram, R.J.; Murty, B.S.; Fabijanic, D.; Suwas, S. Insights into micro-mechanical response and texture of the additively manufactured eutectic high entropy alloy AlCoCrFeNi2.1. *J. Alloys Compd.* **2020**, *827*, 154034. [[CrossRef](#)]
80. Read, N.; Wang, W.; Essa, K.; Attallah, M.M. Selective laser melting of AlSi10Mg alloy: Process optimisation and mechanical properties development. *Mater. Des.* **2015**, *65*, 417–424. [[CrossRef](#)]
81. Javidani, M.; Arreguin-Zavala, J.; Danovitch, J.; Tian, Y.; Brochu, M. Additive Manufacturing of AlSi10Mg Alloy Using Direct Energy Deposition: Microstructure and Hardness Characterization. *J. Therm. Spray Technol.* **2017**, *26*, 587–597. [[CrossRef](#)]
82. Wang, M.; Song, B.; Wei, Q.; Zhang, Y.; Shi, Y. Effects of annealing on the microstructure and mechanical properties of selective laser melted AlSi7Mg alloy. *Mater. Sci. Eng. A* **2019**, *739*, 463–472. [[CrossRef](#)]
83. Rao, J.H.; Zhang, Y.; Zhang, K.; Huang, A.; Davies, C.H.J.; Wu, X. Multiple precipitation pathways in an Al-7Si-0.6Mg alloy fabricated by selective laser melting. *Scr. Mater.* **2019**, *160*, 66–69. [[CrossRef](#)]
84. Leary, M.; Mazur, M.; Elambasseril, J.; McMillan, M.; Chirent, T.; Sun, Y.; Qian, M.; Easton, M.; Brandt, M. Selective laser melting (SLM) of AlSi12Mg lattice structures. *Mater. Des.* **2016**, *98*, 344–357. [[CrossRef](#)]
85. Louvis, E.; Fox, P.; Sutcliffe, C.J. Selective laser melting of aluminium components. *J. Mater. Process. Technol.* **2011**, *211*, 275–284. [[CrossRef](#)]
86. Buchbinder, D.; Meiners, W.; Wissenbach, K.; Müller-Lohmeier, K.; Brandl, E.; Skrynecki, N. *Rapid Manufacturing of Aluminium Parts for Serial Production Via Selective Laser Melting (SLM)*; International Conference on Rapid Manufacturing: Loughborough, UK, 2008.
87. Li, W.; Li, S.; Liu, J.; Zhang, A.; Zhou, Y.; Wei, Q.; Yan, C.; Shi, Y. Effect of heat treatment on AlSi10Mg alloy fabricated by selective laser melting: Microstructure evolution, mechanical properties and fracture mechanism. *Mater. Sci. Eng. A* **2016**, *663*, 116–125. [[CrossRef](#)]
88. Asgari, H.; Baxter, C.; Hosseinkhani, K.; Mohammadi, M. On microstructure and mechanical properties of additively manufactured AlSi10Mg\_200C using recycled powder. *Mater. Sci. Eng. A* **2017**, *707*, 148–158. [[CrossRef](#)]
89. Ansari, P.; Salamci, M.U. On the selective laser melting based additive manufacturing of AlSi10Mg: The process parameter investigation through multiphysics simulation and experimental validation. *J. Alloys Compd.* **2022**, *890*, 161873. [[CrossRef](#)]
90. Trevisan, F.; Calignano, F.; Lorusso, M.; Pakkanen, J.; Aversa, A.; Ambrosio, E.P.; Lombardi, M.; Fino, P.; Manfredi, D. On the selective laser melting (SLM) of the AlSi10Mg alloy: Process, microstructure, and mechanical properties. *Materials* **2017**, *10*, 76. [[CrossRef](#)]
91. Kempen, K.; Thijs, L.; Van Humbeeck, J.; Kruth, J.P. Mechanical Properties of AlSi10Mg Produced by Selective Laser Melting. *Phys. Procedia* **2012**, *39*, 439–446. [[CrossRef](#)]
92. Aboulkhair, N.T.; Maskery, I.; Tuck, C.; Ashcroft, I.; Everitt, N.M. The microstructure and mechanical properties of selectively laser melted AlSi10Mg: The effect of a conventional T6-like heat treatment. *Mater. Sci. Eng. A* **2016**, *667*, 139–146. [[CrossRef](#)]
93. Wang, X.J.; Zhang, L.C.; Fang, M.H.; Sercombe, T.B. The effect of atmosphere on the structure and properties of a selective laser melted Al-12Si alloy. *Mater. Sci. Eng. A* **2014**, *597*, 370–375. [[CrossRef](#)]
94. Wu, J.; Wang, X.Q.; Wang, W.; Attallah, M.M.; Loretto, M.H. Microstructure and strength of selectively laser melted AlSi10Mg. *Acta Mater.* **2016**, *117*, 311–320. [[CrossRef](#)]
95. Van Cauwenbergh, P.; Samae, V.; Thijs, L.; Nejedzlebová, J.; Sedláček, P.; Iveković, A.; Schryvers, D.; Van Hooreweder, B.; Vanmeensel, K. Unravelling the multi-scale structure–property relationship of laser powder bed fusion processed and heat-treated AlSi10Mg. *Sci. Rep.* **2021**, *11*, 6423. [[CrossRef](#)]
96. Kaufman, J.G. *Properties of Aluminum Alloys: Tensile Creep and Fatigue Data at High and Low Temperatures*; ASM International: Almere, The Netherlands, 1999.
97. Lumley, R.N. Technical Data Sheets for Heat-Treated Aluminum High-Pressure Die Castings. *Die Cast. Eng.* **2008**, *32*, 1–36.
98. ASM International Handbook Committee. *Properties and Selection: Nonferrous Alloys and Special-Purpose Materials*; ASM International: Almere, The Netherlands, 1990.
99. Wang, L.; Gao, M.; Zhang, C.; Zeng, X. Effect of beam oscillating pattern on weld characterization of laser welding of AA6061-T6 aluminum alloy. *Mater. Des.* **2016**, *108*, 707–717. [[CrossRef](#)]
100. Fulcher, B.A.; Leigh, D.K.; Watt, T.J. Comparison of ALSI10MG and AL 6061 processed through DMLS. In Proceedings of the 25th Annual International Solid Freeform Fabrication Symposium: An Additive Manufacturing Conference, Austin, TX, USA, 4–6 August 2014; SFF. 2014.
101. Cicală, E.; Duffet, G.; Andrzejewski, H.; Grevey, D.; Ignat, S. Hot cracking in Al-Mg-Si alloy laser welding—Operating parameters and their effects. *Mater. Sci. Eng. A* **2005**, *395*, 1–9. [[CrossRef](#)]
102. Loh, L.E.; Liu, Z.H.; Zhang, D.Q.; Mapar, M.; Sing, S.L.; Chua, C.K.; Yeong, W.Y. Selective Laser Melting of aluminium alloy using a uniform beam profile. *Virtual Phys. Prototyp.* **2014**, *9*, 11–16. [[CrossRef](#)]
103. Ding, Y.; Muñiz-Lerma, J.A.; Trask, M.; Chou, S.; Walker, A.; Brochu, M. Microstructure and mechanical property considerations in additive manufacturing of aluminum alloys. *MRS Bull.* **2016**, *41*, 745–751. [[CrossRef](#)]

104. Zhang, H.; Zhu, H.; Nie, X.; Qi, T.; Hu, Z.; Zeng, X. Fabrication and heat treatment of high strength Al-Cu-Mg alloy processed using selective laser melting. *Laser 3D Manuf. III* **2016**, *9738*, 97380X. [[CrossRef](#)]
105. Olakanmi, E.O.; Cochrane, R.F.; Dalgarano, K.W. A review on selective laser sintering/melting (SLS/SLM) of aluminium alloy powders: Processing, microstructure, and properties. *Prog. Mater. Sci.* **2015**, *74*, 401–477. [[CrossRef](#)]
106. Ghaini, F.M.; Sheikhi, M.; Torkamany, M.J.; Sabbaghzadeh, J. The relation between liquation and solidification cracks in pulsed laser welding of 2024 aluminium alloy. *Mater. Sci. Eng. A* **2009**, *519*, 167–171. [[CrossRef](#)]
107. Pellini, W.S. Strain theory of hot tearing. *Foundry* **1952**, *80*, 125–133.
108. Soysal, T.; Kou, S. A simple test for assessing solidification cracking susceptibility and checking validity of susceptibility prediction. *Acta Mater.* **2018**, *143*, 181–197. [[CrossRef](#)]
109. Xu, R.; Li, R.; Yuan, T.; Niu, P.; Wang, M.; Lin, Z. Microstructure, metallurgical defects and hardness of Al–Cu–Mg–Li–Zr alloy additively manufactured by selective laser melting. *J. Alloys Compd.* **2020**, *835*, 155372. [[CrossRef](#)]
110. Liu, S.; Hong, K.M.; Shin, Y.C. A novel 3D cellular automata-phase field model for computationally efficient dendrite evolution during bulk solidification. *Comput. Mater. Sci.* **2021**, *192*, 110405. [[CrossRef](#)]
111. Liu, S.; Shin, Y.C. Prediction of 3D microstructure and phase distributions of Ti6Al4V built by the directed energy deposition process via combined multi-physics models. *Addit. Manuf.* **2020**, *34*, 101234. [[CrossRef](#)]
112. Katgerman, D.L.; Eskin, D.G. In search of the prediction of hot cracking in aluminium alloys. In *Hot Cracking Phenomena in Welds II*; Springer: Berlin/Heidelberg, Germany, 2008.
113. Fischer, P.; Karapatis, N.; Romano, V.; Glardon, R.; Weber, H.P. A model for the interaction of near-infrared laser pulses with metal powders in selective laser sintering. *Appl. Phys. A Mater. Sci. Process.* **2002**, *74*, 467–474. [[CrossRef](#)]
114. Li, Y.; Gu, D.; Zhang, H.; Xi, L. Effect of Trace Addition of Ceramic on Microstructure Development and Mechanical Properties of Selective Laser Melted AlSi10Mg Alloy. *Chin. J. Mech. Eng.* **2020**, *33*, 33. [[CrossRef](#)]
115. Yang, K.V.; Rometsch, P.; Jarvis, T.; Rao, J.; Cao, S.; Davies, C.; Wu, X. Porosity formation mechanisms and fatigue response in Al-Si-Mg alloys made by selective laser melting. *Mater. Sci. Eng. A* **2018**, *712*, 166–174. [[CrossRef](#)]
116. Weingarten, C.; Buchbinder, D.; Pirch, N.; Meiners, W.; Wissenbach, K.; Poprawe, R. Formation and reduction of hydrogen porosity during selective laser melting of AlSi10Mg. *J. Mater. Process. Technol.* **2015**, *221*, 112–120. [[CrossRef](#)]
117. Dai, D.; Gu, D. Effect of metal vaporization behavior on keyhole-mode surface morphology of selective laser melted composites using different protective atmospheres. *Appl. Surf. Sci.* **2015**, *355*, 310–319. [[CrossRef](#)]
118. Bayoumy, D.; Schliephake, D.; Dietrich, S.; Wu, X.H.; Zhu, Y.M.; Huang, A.J. Intensive processing optimization for achieving strong and ductile Al-Mn-Mg-Sc-Zr alloy produced by selective laser melting. *Mater. Des.* **2021**, *198*, 109317. [[CrossRef](#)]
119. Nie, X.; Zhang, H.; Zhu, H.; Hu, Z.; Zeng, X. The effect of processing parameter on zirconium modified Al-Cu-Mg alloys fabricated by selective laser melting. In *Proceedings of the Solid Freeform Fabrication 2018: Proceedings of the 29th Annual International, Solid Freeform Fabrication Symposium—An Additive Manufacturing Conference*; Austin, TX, USA, 13–15 August 2018; pp. 1246–1252.
120. Maamoun, A.H.; Xue, Y.F.; Elbestawi, M.A.; Veldhuis, S.C. The effect of selective laser melting process parameters on the microstructure and mechanical properties of Al6061 and AlSi10Mg alloys. *Materials* **2018**, *12*, 12. [[CrossRef](#)]
121. Qbau, N.; Nam, N.D.; Ca, N.X.; Hien, N.T. The crack healing effect of scandium in aluminum alloys during laser additive manufacturing. *J. Manuf. Process.* **2020**, *50*, 241–246. [[CrossRef](#)]
122. Lu, Y.; Wu, S.; Gan, Y.; Huang, T.; Yang, C.; Junjie, L.; Lin, J. Study on the microstructure, mechanical property and residual stress of SLM Inconel-718 alloy manufactured by differing island scanning strategy. *Opt. Laser Technol.* **2015**, *75*, 197–206. [[CrossRef](#)]
123. Chen, C.; Yin, J.; Zhu, H.; Xiao, Z.; Zhang, L.; Zeng, X. Effect of overlap rate and pattern on residual stress in selective laser melting. *Int. J. Mach. Tools Manuf.* **2019**, *145*, 103433. [[CrossRef](#)]
124. Sealy, M.P.; Madireddy, G.; Williams, R.E.; Rao, P.; Toursangasarak, M. Hybrid processes in additive manufacturing. *J. Manuf. Sci. Eng. Trans. ASME* **2018**, *140*, 060801. [[CrossRef](#)]
125. Wang, Z.; Oliveira, J.P.; Zeng, Z.; Bu, X.; Peng, B.; Shao, X. Laser beam oscillating welding of 5A06 aluminum alloys: Microstructure, porosity and mechanical properties. *Opt. Laser Technol.* **2019**, *111*, 58–65. [[CrossRef](#)]
126. Yu, W.; Sing, S.L.; Chua, C.K.; Tian, X. Influence of re-melting on surface roughness and porosity of AlSi10Mg parts fabricated by selective laser melting. *J. Alloys Compd.* **2019**, *792*, 574–581. [[CrossRef](#)]
127. Han, Q.; Jiao, Y. Effect of heat treatment and laser surface remelting on AlSi10Mg alloy fabricated by selective laser melting. *Int. J. Adv. Manuf. Technol.* **2019**, *102*, 3315–3324. [[CrossRef](#)]
128. Schmidt, J.; Scholz, R.; Riegel, H. Laser polishing of aluminum by remelting with high energy pulses. *Materwiss. Werksttech.* **2015**, *46*, 686–691. [[CrossRef](#)]
129. Damon, J.; Dietrich, S.; Vollert, F.; Gibmeier, J.; Schulze, V. Process dependent porosity and the influence of shot peening on porosity morphology regarding selective laser melted AlSi10Mg parts. *Addit. Manuf.* **2018**, *20*, 458–464. [[CrossRef](#)]
130. Teng, X.; Zhang, G.; Zhao, Y.; Cui, Y.; Li, L.; Jiang, L. Study on magnetic abrasive finishing of AlSi10Mg alloy prepared by selective laser melting. *Int. J. Adv. Manuf. Technol.* **2019**, *105*, 2513–2521. [[CrossRef](#)]
131. Mahmood, M.A.; Chioibasu, D.; Rehman, A.U.; Mihai, S.; Popescu, A.C. Post-Processing Techniques to Enhance the Quality of Metallic Parts Produced by Additive Manufacturing. *Metals* **2022**, *12*, 77. [[CrossRef](#)]
132. Peng, X.; Kong, L.; Fuh, J.Y.H.; Wang, H. A review of post-processing technologies in additive manufacturing. *J. Manuf. Mater. Process.* **2021**, *5*, 38. [[CrossRef](#)]

133. Shiyas, K.A.; Ramanujam, R. A review on post processing techniques of additively manufactured metal parts for improving the material properties. *Mater. Today Proc.* **2021**, *46*, 1429–1436. [CrossRef]
134. Ye, C.; Zhang, C.; Zhao, J.; Dong, Y. Effects of Post-processing on the Surface Finish, Porosity, Residual Stresses, and Fatigue Performance of Additive Manufactured Metals: A Review. *J. Mater. Eng. Perform.* **2021**, *30*, 6407–6425. [CrossRef] [PubMed]
135. Wang, L.F.; Sun, J.; Yu, X.L.; Shi, Y.; Zhu, X.G.; Cheng, L.Y.; Liang, H.H.; Yan, B.; Guo, L.J. Enhancement in mechanical properties of selectively laser-melted AlSi10Mg aluminum alloys by T6-like heat treatment. *Mater. Sci. Eng. A* **2018**, *734*, 299–310. [CrossRef]
136. Schuster, M.; De Luca, A.; Widmer, R.; Maeder, X.; Leinenbach, C. Processability, microstructure and precipitation of a Zr-modified 2618 aluminium alloy fabricated by laser powder bed fusion. *J. Alloys Compd.* **2022**, *913*, 165346. [CrossRef]
137. Maamoun, A.H.; Elbestawi, M.; Dosbaeva, G.K.; Veldhuis, S.C. Thermal post-processing of AlSi10Mg parts produced by Selective Laser Melting using recycled powder. *Addit. Manuf.* **2018**, *21*, 234–247. [CrossRef]
138. Otani, Y.; Sasaki, S. Effects of the addition of silicon to 7075 aluminum alloy on microstructure, mechanical properties, and selective laser melting processability. *Mater. Sci. Eng. A* **2020**, *777*, 139079. [CrossRef]
139. Zhang, J.; Gao, J.; Song, B.; Zhang, L.; Han, C.; Cai, C.; Zhou, K.; Shi, Y. A novel crack-free Ti-modified Al-Cu-Mg alloy designed for selective laser melting. *Addit. Manuf.* **2021**, *38*, 101829. [CrossRef]
140. Li, X.; Li, G.; Zhang, M.X.; Zhu, Q. Novel approach to additively manufacture high-strength Al alloys by laser powder bed fusion through addition of hybrid grain refiners. *Addit. Manuf.* **2021**, *48*, 102400. [CrossRef]
141. Wang, Y.; Lin, X.; Kang, N.; Wang, Z.; Liu, Y.; Huang, W. Influence of post-heat treatment on the microstructure and mechanical properties of Al-Cu-Mg-Zr alloy manufactured by selective laser melting. *J. Mater. Sci. Technol.* **2022**, *111*, 35–48. [CrossRef]
142. Nie, X.; Zhang, H.; Zhu, H.; Hu, Z.; Ke, L.; Zeng, X. Effect of Zr content on formability, microstructure and mechanical properties of selective laser melted Zr modified Al-4.24Cu-1.97Mg-0.56Mn alloys. *J. Alloys Compd.* **2018**, *764*, 977–986. [CrossRef]
143. Zhou, L.; Pan, H.; Hyer, H.; Park, S.; Bai, Y.; McWilliams, B.; Cho, K.; Sohn, Y. Microstructure and tensile property of a novel AlZnMgScZr alloy additively manufactured by gas atomization and laser powder bed fusion. *Scr. Mater.* **2019**, *158*, 24–28. [CrossRef]
144. Koutny, D.; Skulina, D.; Pantélejev, L.; Paloušek, D.; Lenczowski, B.; Palm, F.; Nick, A. Processing of Al-Sc aluminum alloy using SLM technology. *Procedia CIRP* **2018**, *74*, 44–48. [CrossRef]
145. Qi, T.; Zhu, H.; Zeng, X.; Yin, J. Effect of Si content on the cracking behavior of selective laser melted Al7050. *Rapid Prototyp. J.* **2019**, *25*, 1592–1600. [CrossRef]
146. John, E. *Hatch Aluminum: Properties and Physical Metallurgy*; ASM International: Almere, The Netherlands, 1984.
147. Gäumann, M.; Trivedi, R.; Kurz, W. Nucleation ahead of the advancing interface in directional solidification. *Mater. Sci. Eng. A* **1997**, *226*, 763–769. [CrossRef]
148. Men, H.; Fan, Z. Effects of solute content on grain refinement in an isothermal melt. *Acta Mater.* **2011**, *59*, 2704–2712. [CrossRef]
149. Zedalis, M.; Fine, M.E. Lattice parameter variation of Al<sub>3</sub>(Ti, V, Zr, Hf) in Al-2 AT.% (Ti, V, Zr, Hf) alloys. *Scr. Metall.* **1983**, *17*, 1247–1251. [CrossRef]
150. Wang, P.; Gammer, C.; Brenne, F.; Niendorf, T.; Eckert, J.; Scudino, S. A heat treatable TiB<sub>2</sub>/Al-3.5Cu-1.5Mg-1Si composite fabricated by selective laser melting: Microstructure, heat treatment and mechanical properties. *Compos. Part B Eng.* **2018**, *147*, 162–168. [CrossRef]
151. Zhang, J.; Yuan, W.; Song, B.; Yin, S.; Wang, X.; Wei, Q.; Shi, Y. Towards understanding metallurgical defect formation of selective laser melted wrought aluminum alloys. *Adv. Powder Mater.* **2022**, *1*, 100035. [CrossRef]
152. Nicholls, R.J.; Ni, N.; Lozano-Perez, S.; London, A.; McComb, D.W.; Nellist, P.D.; Grovenor, C.R.M.; Pickard, C.J.; Yates, J.R. Crystal structure of the ZrO phase at zirconium/zirconium oxide interfaces. *Adv. Eng. Mater.* **2015**, *17*, 211–215. [CrossRef]
153. Opprecht, M.; Garandet, J.P.; Roux, G.; Flament, C.; Soulier, M. A solution to the hot cracking problem for aluminium alloys manufactured by laser beam melting. *Acta Mater.* **2020**, *197*, 40–53. [CrossRef]
154. Martin, J.H.; Yahata, B.D.; Hundley, J.M.; Mayer, J.A.; Schaeder, T.A.; Pollock, T.M. 3D printing of high-strength aluminium alloys. *Nature* **2017**, *549*, 365–369. [CrossRef] [PubMed]
155. Zakharov, V.V. Effect of scandium on the structure and properties of aluminum alloys. *Met. Sci. Heat Treat.* **2003**, *45*, 246–253. [CrossRef]
156. Bi, J.; Lei, Z.; Chen, Y.; Chen, X.; Tian, Z.; Liang, J.; Zhang, X.; Qin, X. Microstructure and mechanical properties of a novel Sc and Zr modified 7075 aluminum alloy prepared by selective laser melting. *Mater. Sci. Eng. A* **2019**, *768*, 138478. [CrossRef]
157. Wang, P.; Yang, Y.; Moghaddam, N.S. Process modeling in laser powder bed fusion towards defect detection and quality control via machine learning: The state-of-the-art and research challenges. *J. Manuf. Process.* **2022**, *73*, 961–984. [CrossRef]
158. Fu, Y.; Downey, A.R.J.; Yuan, L.; Zhang, T.; Pratt, A.; Balogun, Y. Machine learning algorithms for defect detection in metal laser-based additive manufacturing: A review. *J. Manuf. Process.* **2022**, *75*, 693–710. [CrossRef]
159. Barrionuevo, G.O.; Ramos-Grez, J.A.; Walczak, M.; Betancourt, C.A. Comparative evaluation of supervised machine learning algorithms in the prediction of the relative density of 316L stainless steel fabricated by selective laser melting. *Int. J. Adv. Manuf. Technol.* **2021**, *113*, 419–433. [CrossRef]
160. Aoyagi, K.; Wang, H.; Sudo, H.; Chiba, A. Simple method to construct process maps for additive manufacturing using a support vector machine. *Addit. Manuf.* **2019**, *27*, 353–362. [CrossRef]

161. Liu, Q.; Wu, H.; Paul, M.J.; He, P.; Peng, Z.; Gludovatz, B.; Kruzic, J.J.; Wang, C.H.; Li, X. Machine-learning assisted laser powder bed fusion process optimization for AlSi10Mg: New microstructure description indices and fracture mechanisms. *Acta Mater.* **2020**, *201*, 316–328. [[CrossRef](#)]
162. Paulson, N.H.; Gould, B.; Wolff, S.J.; Stan, M.; Greco, A.C. Correlations between thermal history and keyhole porosity in laser powder bed fusion. *Addit. Manuf.* **2020**, *34*, 101213. [[CrossRef](#)]
163. Muhammad, W.; Brahme, A.P.; Ibragimova, O.; Kang, J.; Inal, K. A machine learning framework to predict local strain distribution and the evolution of plastic anisotropy & fracture in additively manufactured alloys. *Int. J. Plast.* **2021**, *136*, 102867. [[CrossRef](#)]
164. Fang, L.; Cheng, L.; Glerum, J.A.; Bennett, J.; Cao, J.; Wagner, G.J. Data-driven analysis of process, structure, and properties of additively manufactured Inconel 718 thin walls. *NPJ Comput. Mater.* **2022**, *8*, 126. [[CrossRef](#)]